THE STATIC AND DYNAMIC PROPERTIES OF SEMICOHERENT INTERFACES IN Cu-Zn-Sn ALLOYS

THE STATIC AND DYNAMIC PROPERTIES OF SEMICOHERENT INTERFACES IN Cu-Zn-Sn ALLOYS

by

DAVID ROBERTSON, B.Sc.

A Thesis

Submitted to the Faculty of Graduate Studies

in Partial Fulfilment of the Requirements

for the Degree

Master of Science

McMaster University

September 1968

MASTER OF SCIENCE
(Metallurgy)

McMASTER UNIVERSITY
Hamilton, Ontario

TITLE: The Static and Dynamic Properties of Semicoherent Interfaces in Cu-Zn-Sn Alloys

AUTHOR: David Robertson, B.Sc.

SUPERVISOR: Dr. G. R. Purdy

NUMBER OF PAGES: (vi); 88

SCOPE AND CONTENTS:

The equilibrium and kinetic properites of semicoherent interfaces between γ precipitates and β matrix in Cu-Zn-Sn are examined using a simple dislocation model. The predicted surface energies and mobilities are compared to those observed in experiments which also assess the validity of current theories of interfacial stability in diffusion-controlled growth.

ACKNOWLEDGMENTS

The author wishes to express his gratitude to Dr. G. R. Purdy for suggesting the problem and guiding it through to its conclusion and to Dr. J. D. Embury who offered ideas and advice concerning dislocation behaviour. Thanks are also extended to the technical staff for their patient assistance in the electron microscopy phase of this work and to the National Research Council of Canada who provided financial support.

TABLE OF CONTENTS

LIST OF TABLES

LIST OF ILLUSTRATIONS

CHAPTER I

INTRODUCTION

It is the purpose of this work to examine the static and dynamic properties of a semicoherent solid-solid interface and to compare these with the predictions of a simple dislocation model. To provide a basis for this, it is necessary to review some of the fundamental definitions and relationships pertaining to solid-solid interfaces in general.

An interface could be defined as the surface corresponding to a particularly rapid spatial rate of change of properties such as orientation, composition, or crystal structure. Interfaces are characterized by the magnitude of the rate of change: in sharp surfaces the change is accomplished over one atomic distance while the change may be spread over several atomic distances for diffuse surfaces. A twin boundary would be an example of a sharp interface while a high-angle grain boundary typifies the diffuse interface. The Bloch walls separating ferromagnetic domains are diffuse interfaces separating regions of different magnetization vector (1).

Because of the property differences or because of the disorder at the surface, an interface has an energy associated with it different from the energy associated with a hypothetical surface of identical shape and orientation lying in a bulk phase. The change in excess Gibbs free energy of the system per unit area of interface created is called the specific surface free energy; this will be denoted by the symbol γ and

will frequently be referred to as "surface energy", although this should not be confused with the true surface energy $\int\int \gamma dA$. Mullins (2) correctly distinguishes between surface energy (or surface tension) a scalar quantity, and surface stress which is a tensor. For fluids, the magnitude of the (isotropic) surface stresses is numerically equal to the magnitude of γ when expressed in suitable units. For solids, neither surface stresses nor surface energy is necessarily isotropic. In fact, the polar plot of γ versus interface orientation frequently contains pointed minima or cusps. The Gibbs-Wulff plot (or γ-plot) is constructed by setting the radius vector $\underline{r}$ equal to $\underline{n}\gamma(\underline{n})$ where $\underline{n}$ is the unit vector normal to the interface. There is also an inverse γ-plot in which $\underline{r}$ is set equal to $\underline{n}\gamma^{-1}(\underline{n})$. For most purposes the former construction is quite adequate. The cusps correspond to orientations at which mismatch across the interface is minimized. By definition, a singular interface is one lying in a cusp orientation. All others are non-singular. Interfaces can further be categorized as coherent, semicoherent, or incoherent depending on the degree of matching between atoms on either side of the surface. When there is continuity of lattice planes across the interface, it is said to be coherent. When there are large areas of coherency separated by localized regions of discontinuity, the interface is said to be semicoherent, and when there is little or no continuity across the interface, it is called incoherent; (note that the degree of coherency does not relate to the degree of sharpness).

When the orientation of the lattice bears some simple (rational) relation to that of the other, the degree of coherency may be maximized. Such a situation leads to an anisotropic surface energy with cusps (singularities) for planes of particularly good matching. On the other hand,

randomly oriented crystals frequently have incoherent, and therefore, non-singular interfaces at all orientations.

In its equilibrium state, a crystal of one phase in a matrix of another will assume the shape required to minimize the total surface free energy. Mullins (2) repeats a proof due to Wulff that this shape is that defined by the innermost envelope of planes normal to the tips of radius vectors in the γ-plot.

This is illustrated for the cases of deep and shallow cusps in Figure 1. Johnson (3) has recently extended the Wulff theorem to include crystals lacking a centre of symmetry but the construction remains basically the same as outlined above.

As the temperature of the system increases, the energies of singular interfaces increase relative to that of nonsingular ones and as the melting point is approached, the γ-plot becomes more spherical. For liquids, it is a sphere.

One deduces that the equilibrium shape of an isolated incoherent crystal in a solid matrix is a sphere while stress-free coherent and semicoherent crystals are bounded by facets corresponding to singular planes. Not all flat faces are singular, however. In a non-equilibrium situation, some may be flat because of low mobility and, of course, when two precipitates impinge a flat grain boundary may result. This leads to the topic of morphologies in general.

Equilibrium morphologies are determined solely by the properties of the γ-plot; growth morphologies reflect conditions of growth such as mobility, surface diffusion, supersaturation, elastic strains, and reaction kinetics. The mobility of an interface is defined as its

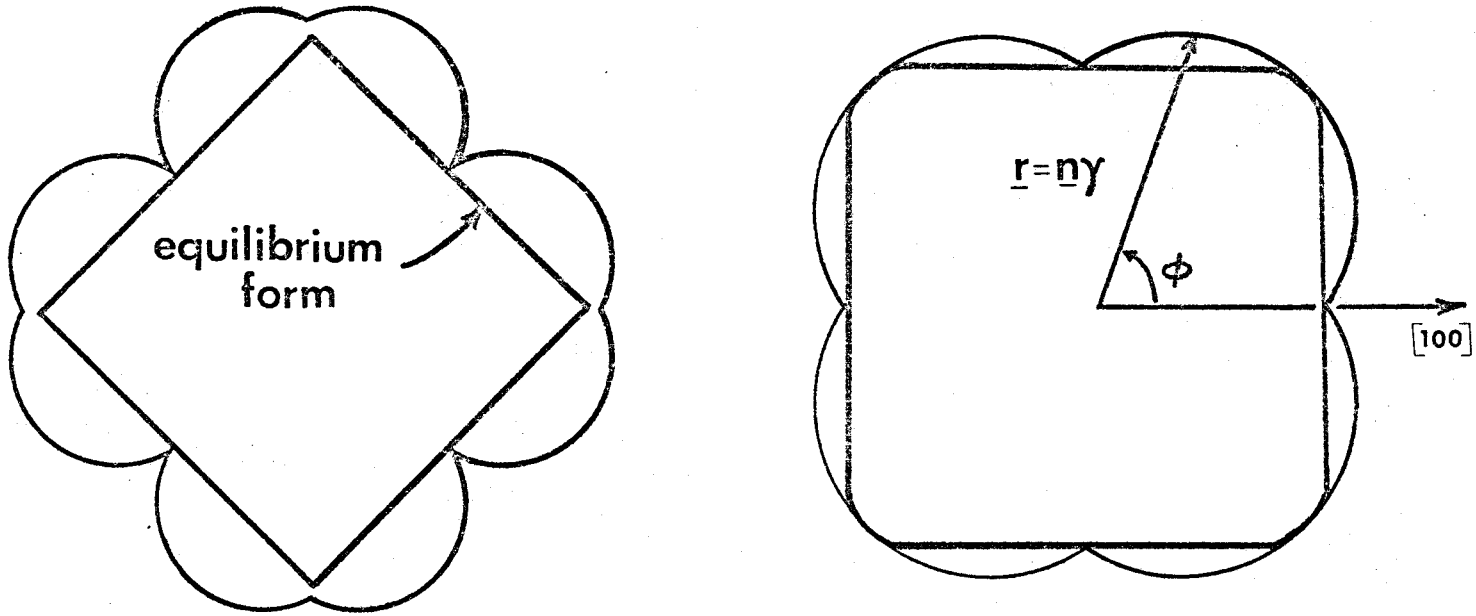

Figure 1. Wulff Plots

velocity relative to the thermodynamic driving force for interface advance. This quantity is fundamentally distinct from the instability propensity of a surface which is a measure of the driving force necessary to cause an initially planar interface to break down during growth. In the experimental work presented here, the observation of instability is taken to imply high mobility. But the converse is not necessarily true since it is shown by Shewmon (4) and Cahn (5) that, in the early stages of growth, when reaction kinetics control the rate of transformation, an interface may well be mobile and yet show no sign of instability since the reaction reduces the solute gradient in the matrix.

Dubé and Aaronson (6,7) have attempted to classify the morphologies of second-phase crystals as:

(a) grain boundary allotriomorphs - crystals nucleated at and growing smoothly along grain boundaries.

(b) Widmanstätten sideplates which grow into a matrix grain either from allotriomorphs (secondary) or directly from the grain boundary (primary).

(c) Widmanstätten sawteeth which are like sideplates but are more equilateral.

(d) idiomorphs - roughly equiaxed crystals growing either in the interior of grains or at their boundaries.

(e) intragranular Widmanstätten plates growing in grain interiors, and finally,

(f) the massive structure resulting from mutual impingement. These types are illustrated in Figure 2.

Figure 2. The Dubé Morphologies

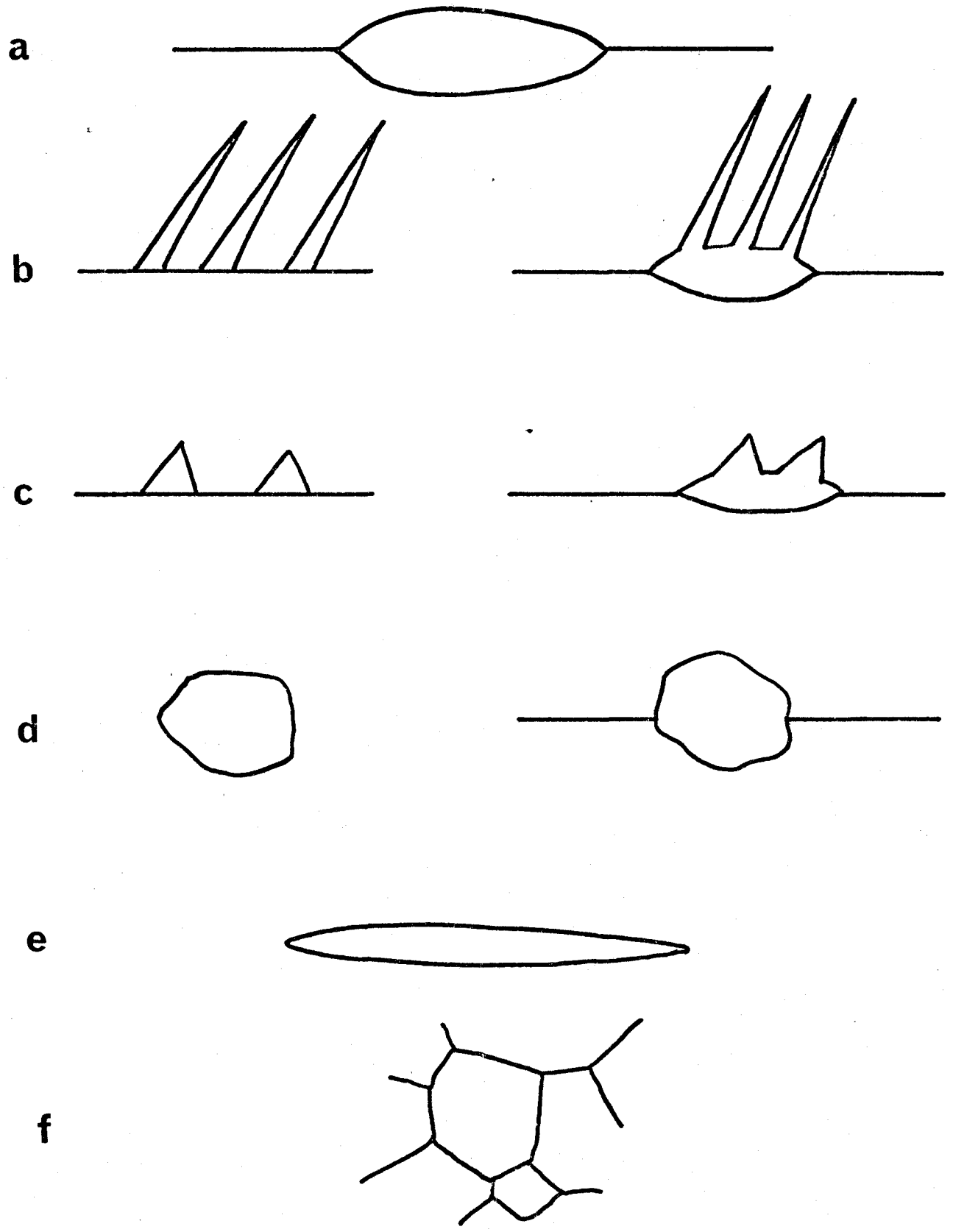

In view of the number of observations of dendritic morphology reported, it must be noted that the Dubé classification is by no means complete. As early as 1931, Mehl and Marzke (8) reported the formation of "stars" of γ-brass precipitated from β on slow cooling which they decided were Widmanstätten figures because of a fixed orientation relationship between star axes and matrix. Kelly and Nicholson (9) review the observation (by McLean and Hale) of dendritic ε-carbide precipitates in Fe-0.23 pct. C quenched and aged at 100°C. They comment that "the majority of dendrites consisted of small plates of ε-carbide growing along $\langle 100 \rangle_{Fe}$ in $\{100\}_{Fe}$ planes". Others with different orientations were discovered to be cementite. For a number of years Massalski and co-workers (10,11) have been observing dendritic morphologies in precipitates of γ from β in Cu-Ga and Cu-Ga-X and Malcolm and Purdy (12) observed dendritic precipitation of γ from β in Cu-Zn-Sn which they rationalized using an interface stability argument. It appears then that dendrites are not uncommon morphology and deserve a place in the Dube scheme.

It is believed that growth morphology is strongly influenced by the mode of growth. One may distinguish two general types. An interface may advance by the lateral growth of surface steps or by uniform motion normal to itself. It was thought that singular interfaces must advance by lateral growth while nonsingular surfaces could continuously advance normal to themselves.

Cahn (1) points out that the criterion for lateral growth is that the surface must reside in a metastable equilibrium configuration in the presence of a driving force after and before the passage of a step. "If the surface cannot reach equilibrium in the presence of the driving force,

then it will continue to advance without waiting for the lateral motion of steps" whether it is singular or not. Given a large enough driving force, any interface can migrate normal to itself.

The tendency to remain planar must clearly be greater when lateral growth obtains. A now-notorious hypothesis by C. S. Smith (13) suggested that under low driving force conditions a precipitate nucleating at a grain boundary would be coherent with one grain but would grow preferentially into the other. The nucleation of coherent particles is indeed favoured due to the lower free energy of nucleation and it was supposed that growth should proceed more rapidly into the incoherent grain because the more disordered incoherent interface has a higher mobility than the coherent one. Indeed, early experiments on Cu-Ag and proeutectoid ferrite seemed to verify Smith's hypothesis but as Aaronson (7) shows, proeutectoid ferrite can grow into its coherent neighbour, its incoherent neighbour, or both at the same time. The reasoning is that while an incoherent surface is more mobile, a coherent surface usually has a smaller surface free energy and is energetically favoured.

The motion of a semicoherent interface requires ledge motion or synchronous climb of the dislocations formed to accommodate the mismatch. In either case, this should be significantly slower than the direct transfer of atoms across an incoherent interface. The recent investigations by Clark (14) of growth morphologies of primary sawteeth in Fe-C rationalize the growth of flat faces by taking them to be semicoherent surfaces advancing much more slowly than the more disordered surfaces and therefore, increasing in extent.

The growth of Widmanstätten figures has been explained (7) as due to the minimization of volume strain energy for plates coupled with the point effect of diffusion at plate edges. Allotriomorphs can be said to grow along grain boundaries since their presence leads to an overall reduction in surface energy. By comparison, grain boundary idiomorphs do not "wet" the grain boundaries and remain spheroidal.

There have been a few recent investigations of growth details. Hren and Thomas (15) have followed the precipitation process in Al-20 pct Ag in the hot stage of an electron microscope. They observed that unit dislocations in fcc split into partials to accommodate growth of the hcp precipitate and that the interface had the properties of a stacking fault. Lengthening of plates required only the motion of $\frac{a}{6}$ <112> partials while thickening demanded creation of new partial dislocations. It is not unexpected that the precipitates grow to long, narrow lenticular plates since nucleation of new partials requires considerable volume strain to activate sources.

Laird and Aaronson (16) determined the dislocation structures of the broad faces of Widmanstätten plates in Al-15 pct Ag. They verify that the dislocations are $\frac{a}{6}$ <112> but note that, initially there is only one set and later two and three sets of dislocations in keeping with a prediction that the triple net should be the most stable configuration. They suggest that ledge motion is required but Hren and Thomas would consider the partial itself as the ledge.

In a more recent work, Laird and Aaronson (17) turned to an examination of the broad surfaces of θ' in Al-4 pct Cu. They concluded that the broad surfaces are fully coherent and the dislocations observed on

them were "intruders" resulting from plastic strain or else misfit dislocations corresponding to ledges. They definitely identified misfit dislocations taking up the one-dimensional strain at the plate edges as loops which polygonized during growth but which were circular during dissolution (probably because of differing driving forces). Their measured growth rates were significantly slower than that predicted by volume diffusion suggesting that a ledge mechanism was at work and that the "intruder" dislocations act as ledge sources.

Using transmission electron microscopy of thin foils, Nicholson and Weatherly (18) have determined the dislocation structure of semicoherent interfaces bounding precipitates of θ' in Al-Cu, S in Al-Cu-Mg, β' in Al-Mg-Si, and γ' in Ni-Cu-Ti-Al. Because γ' has low misfit in all directions the growth form is a sphere bounded by hexagonal nets of $\frac{a}{2}$ <110> dislocations. The spheres are observed to lose coherency by attracting matrix dislocations which climb and react to yield a suitable network. Cube oriented θ' in α-Al has low misfit in two cube directions and therefore grows as discs. The authors confirm Laird and Aaronson's observation of a (001) accommodation dislocation at plate edges, and the glissile $\frac{a}{2}$[110] "intruders" resulting from deformation of the foil but also observe dislocations accommodating misfit on the flat faces. Further, they observed that coherency was lost by the nucleation of loops within the precipitate followed by climb to the interface. Needles and laths were formed in β' and S because of good matching along an [001] direction. The misfit dislocations were $\frac{a}{2}$[101] loops formed when a matrix dislocation transformed to helices about the precipitate and subsequently decomposed into loops and another matrix dislocation. The work of Nicholson and

and Weatherly clearly demonstrates the complexity of the situation, pointing out the need for investigations similar to theirs in other systems.

To conclude this introduction, a very brief description of the interface stability theory will be presented. Probably the best place to start is at the works of Mullins and Sekerka (19,20). For a spherical particle undergoing diffusion-controlled or thermally-controlled growth they first applied an infinitesimal perturbation so that the surface of the body was defined by

$$r = \rho(\Theta,\phi) = R + \delta Y_{\ell m} \qquad (1.1)$$

where R is the average radius, δ is an amplitude, and $Y_{\ell m}$ is a normalized spherical harmonic and the quantities R and δ are time-dependent. The surface concentration c_s is related to the equilibrium concentration c_o, mean curvature K, and capillarity constant Γ (equal to $\gamma\Omega/kT$ for surface energy γ and atomic volume Ω) through the Gibbs-Thomson equation as:

$$c_s = c_o + c_o \Gamma K \qquad (1.2)$$

The general solution to Laplace's equation for spherical symmetry applies to steady state growth and Coriell and Parker (21) have justified this as an approximation to the time-dependent solution for positions near the interface. Integration constants are evaluated using equation (1.2). They calculate the growth rate of amplitude from a mass balance:

$$v = \frac{dR}{dt} + Y_{\ell m} \frac{d\delta}{dt} = \frac{D}{C-c_s} \left(\frac{\partial c}{\partial r}\right)_{r=\rho} \qquad (1.3)$$

The growth rate of the $\ell^{\underline{th}}$ harmonic is:

$$\frac{\dot{\delta}_\ell}{\delta_\ell} = \frac{D(\ell-1)}{R(C-c_R)} \left[G - \frac{C_o \Gamma}{R^2}(\ell+1)(\ell+2)\right] \qquad (1.4)$$

where C is the precipitate concentration and c_R is the concentration on an undistorted sphere of radius R. It is seen that a large solute gradient G favours growth of the perturbation while capillarity opposes growth. One can determine for what values of R a growing sphere will be stable with respect to a given perturbation. Generally, small spheres are stable because of the effectively larger capillarity term and all spheres are more stable as the supersaturation is decreased.

Coriell and Parker (21,22) perform a similar calculation for cylindrical geometry and include a reaction kinetics term by equating the growth velocity v to a function of supersaturation of the form $k(C_\infty - C_o)^m$. When reaction control dominates, spheres are stable to very much larger radii. Cahn (5) has treated the effect of interface kinetics for both normal and lateral growth mechanisms. Kinetics tends to reduce the gradients G in the matrix particularly for small radii and the onset of instability coincides with the onset of diffusion-controlled growth. In the same paper, Cahn employed an anisotropic surface free energy and concluded that anisotropic surface energy "is not effective at all, and will force the instability to reflect the anisotropy". This is support for the belief that oriented, semi-coherent precipitates are naturally less stable against perturbation.

In 1965, Shewmon (4) concentrated on solid-solid transformations, showing the stabilizing influence of reaction kinetics as well as examining

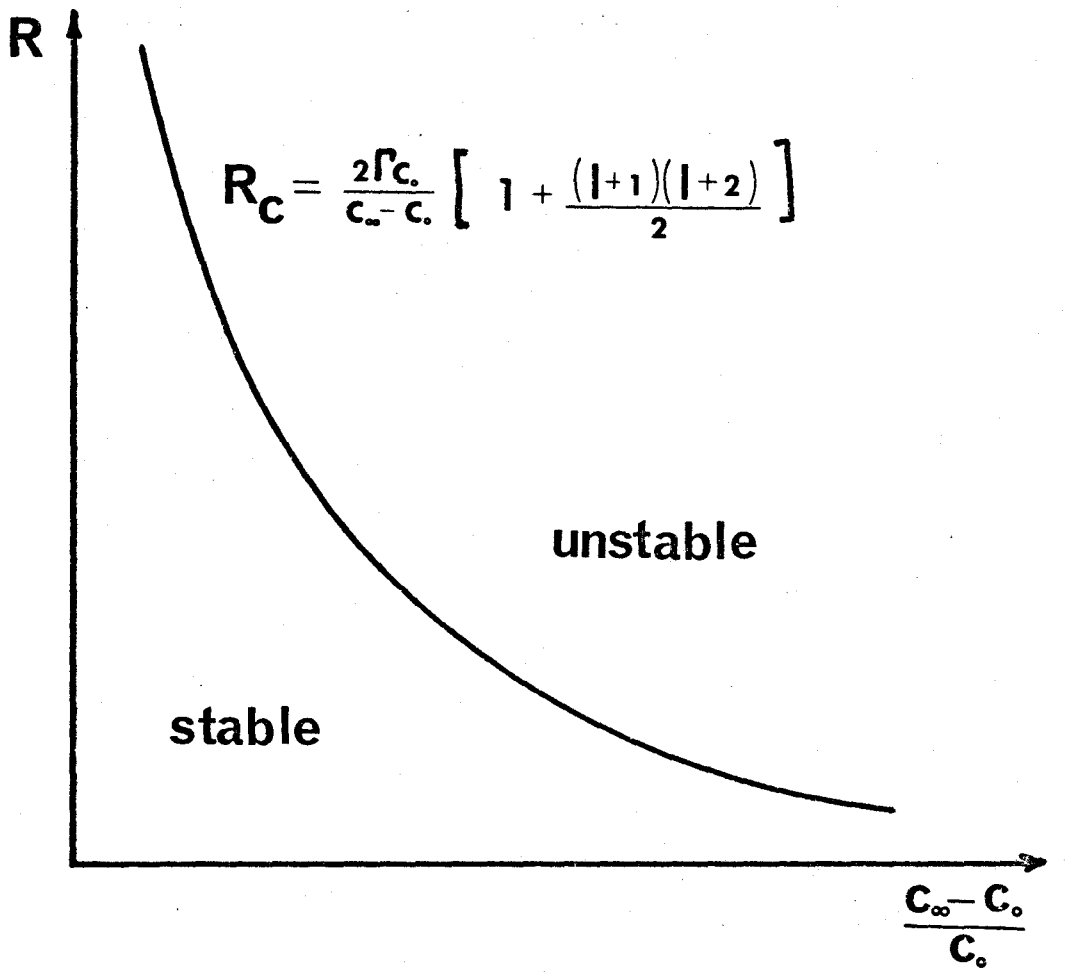

Figure 3. Region of Stability for a Sphere

the effect of other solute species and strain energy. If one solute diffuses much more slowly than the other, stability should prevail since gradients will be reduced. He also concludes that the stabilizing effect of strain energy is small when vacancy sources are within diffusion range of the interface. This topic will be discussed at length in a later section.

Lately, Sekerka (23) and Delves (24) have undertaken the time-dependent analysis of perturbation development. Sekerka treats a planar interface moving at constant velocity v being perturbed by a function $\phi(x,t)$. After splitting the concentration into a steady-state part and a time dependent part, he employs Laplace transforms and Fourier transforms, eventually arriving at the conclusion that instability obtains when the perturbation wavelength

$$\lambda > 2\pi \left(\frac{c_o}{C-c_o} \Gamma \frac{D}{v} \right)^{1/2} \equiv \lambda_o \qquad (1.5)$$

The value of Λ (ie. λ/λ_o) for the fastest-growing perturbation is defined in terms of the parameter

$$\eta = \frac{4\pi D}{V\lambda_o} \qquad (1.6)$$

as

$$\eta^2 = \frac{4(\Lambda_c^2-2)}{\Lambda_c^2(\Lambda_c^2-3)^2} \qquad (1.7)$$

It turns out that Λ_c is always greater than $\sqrt{3}$ whereas the Laplace equation predicts that Λ_c equals $\sqrt{3}$ and the steady-state equation predicts Λ_c lies between $\sqrt{2}$ and $\sqrt{3}$. For $\eta \geq 1$ corresponding to slow growth, all three theories yield the value $\sqrt{3}$. Finally, Sekerka presents a solved time evolution showing how several instabilities develop from one initial

shape to the final morphology. Truthfully, the theory only applies to steady-state growth but should not be a bad approximation to the real case for long growth times and will later be used to estimate the magnitude of γ in Cu-Zn-Sn precipitates.

Only a few experiments have been performed to test the theory but these show fair agreement. Hardy and Coriell (25) have actually measured the growth rate of perturbations relative to the radius of an ice cylinder. They report agreement with the theory to within 25%.

Measurements of dendrite arm spacings by Malcolm and Purdy (12) yielded a value for the surface energy of about 50 ergs/cm^2 in β/γ Cu-Zn-Sn. This figure seems to agree well with the values estimated in the present work.

Morris and Winegard (26) have observed the growth of a dendrite tip in camphor-succinonitrile solutions. In uniform cycles, the tip grows more and more bulbous, finally developing a new set of side branches and beginning a new cycle. Treating the tip as an isolated growing sphere one may relate these events to the theory: A certain size must be exceeded before breakdown occurs.

Overall, many more experiments are required to fully evaluate the applicability of the various theories. It is hoped that the following results may be the source of some enlightenment.

CHAPTER 2

STATIC PROPERTIES OF SEMICOHERENT INTERFACES

Woo, Barrett and Mehl (27) determined that the orientation relationship between β and γ brass is;

$$(100)_\beta \parallel (100)_\gamma \qquad (2.1)$$
$$[100]_\beta \parallel [100]_\gamma$$

This, coupled with the near-equality of lattice spacings leads one to expect semicoherent interfaces. Because of the slight difference in lattice parameters, strain would build up to unbearable values unless relieved by edge dislocations spaced at a distance

$$\lambda = \frac{b_\gamma \cdot b_\beta}{b_\gamma - b_\beta} \qquad (2.2)$$

as sketched in Figure 4.

The type of dislocations required to accommodate the misfit would appear to be pure edge with Burgers vectors lying in the interface plane. However, dislocations can react to form energetically more stable networks such as was reported by Laird and Aaronson. The equilibrium configuration will be that which accommodates the misfit while producing the least interfacial energy.

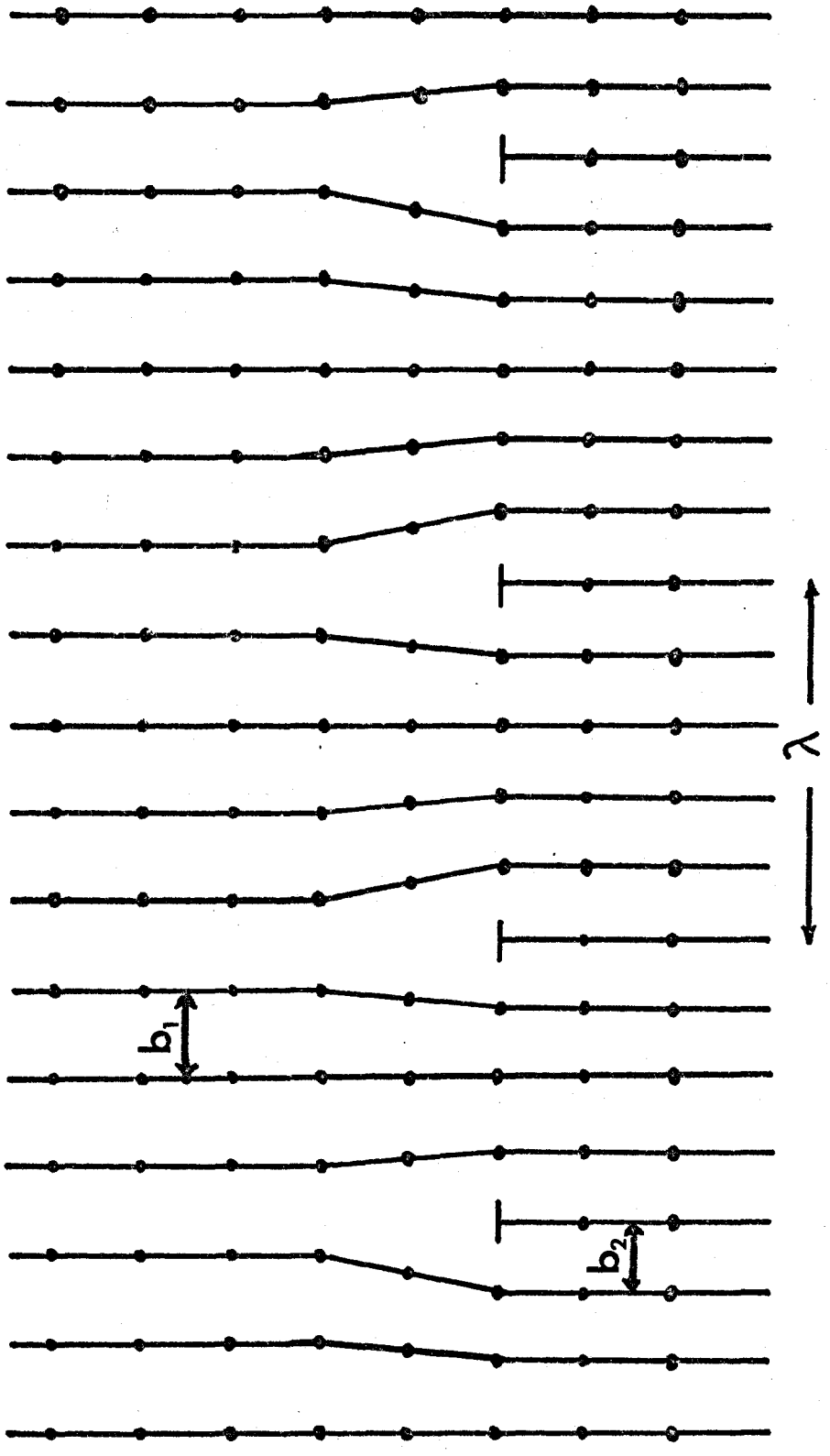

Figure 4. Interface Model

2.1 Interfacial Energy

As Turnbull (28) states, the specific free surface energy can be written as the sum of a chemical term γ_c and a mechanical term γ_m. In what follows, the chemical term is estimated from a Zeroth Order calculation and the mechanical term is calculated using isotropic and anisotropic elasticity and a Frenkel-Kontorova computation in which the dislocations are effectively "smeared" rather than discrete entities. With these results, a γ-plot can be constructed and compared with some of the equilibrium forms observed to assess the validity of the theory.

Chemical Energy

Let the atom fraction of species i in phase α be x_i^α. Let each atom at the interface have Z bonds with atoms in the next phase. Put n atoms per unit area at the interface and consider unit area.

The number of 1 atoms in γ is nX_1^γ and there are nX_2^γ of type 2. Each atom of type i in γ "sees" Z neighbours in β. The numbers of each kind are Zx_1^β and Zx_2^β.

For type 1 atoms in γ the bond energy is

$$\varepsilon_{11} Z n x_1^\gamma x_1^\beta + \varepsilon_{12} Z n x_1^\gamma x_2^\beta \qquad (2.3)$$

For type 2 atoms in γ it is

$$\varepsilon_{12} Z n x_2^\gamma x_1^\beta + \varepsilon_{22} Z n x_2^\gamma x_2^\beta \qquad (2.4)$$

The total is

$$U(\gamma|\beta) = Zn\,[\varepsilon_{11} x_1^\gamma x_1^\beta + \varepsilon_{12}(x_1^\gamma x_2^\beta + x_2^\gamma x_1^\beta) + \varepsilon_{22} x_2^\gamma x_2^\beta] \qquad (2.5)$$

Consider a $\gamma|\gamma$ boundary. Replace β in (2.5) with γ.

$$U(\gamma|\gamma) = Zn\,[\varepsilon_{11}x_1^{\gamma}x_1^{\gamma} + 2\varepsilon_{12}(x_1^{\gamma}x_2^{\gamma}) + \varepsilon_{22}x_2^{\gamma}x_2^{\gamma}] \qquad (2.6)$$

For a $\beta|\beta$ boundary, one obtains

$$U(\beta|\beta) = Zn\,[\varepsilon_{11}x_1^{\beta}x_1^{\beta} + 2\varepsilon_{12}(x_1^{\beta}x_2^{\beta}) + \varepsilon_{22}x_2^{\beta}x_2^{\beta}] \qquad (2.7)$$

Taking as a reference state the surface between halves of a single crystal, the excess energy per unit area of the bicrystal system is γ_c.

$$\gamma_c = U_{(\gamma|\beta)} - \frac{1}{2}\,[U_{(\beta|\beta)} + U_{(\gamma|\gamma)}]$$

$$= Zn\,(x_2^{\gamma} - x_2^{\beta})^2\,[\varepsilon_{12} - \frac{1}{2}\,(\varepsilon_{11} + \varepsilon_{22})] \qquad (2.8)$$

The familiar quantity in the square brackets is ω related to the critical ordering temperature T_c by

$$\omega = -\frac{1}{2}\,k\,T_c \qquad (2.9)$$

where k is Boltzmann's constant.

For (100) and (110) planes in a b.c.c. structure of parameter a, nZ takes the values $8/a^2$ and $5.656/a^2$ respectively.

Since T_c is $740^{\circ}K$, ω is estimated at -5.11×10^{-14} ergs. Taking

$$a = 2.95 \times 10^{-8}\ \text{cm} \qquad \text{and}$$

$$x_2^{\gamma} = 0.575 \qquad \text{and } x_2^{\beta} \simeq 0.485\ ,$$

one arrives at a value for γ_c, namely 3.7 and 2.6 ergs/cm^2 respectively. This is quite a small value and reflects the chemical similarity of β to γ brass.

Mechanical Energy

It will be assumed that the interface contains a two-dimensional network of dislocations of Burgers vector $\underline{b} = (b_1, b_2, b_3)$ referred to axes lying in the interface and normal to it. The mechanical energy term is then the self-energy plus interaction energy of dislocations per unit area. The total energy per unit length of each dislocation is ξ which can be written (29)

$$\xi = \xi^o + \frac{[K_{11}\ (b_1^2 + b_2^2) + K_{33}\ (b_3^2)]}{4\pi} \ln \frac{R}{r_o} \qquad (2.10)$$

The dislocation line forms one of the axes in the surface. The inelastic core energy ξ^o is usually taken as $C_{44}\ a^2/10$ on the assumption that the core stresses approach the theoretical shear strength $C_{44}/30$. R and r_o are the outer and inner cut off radii taken as the spacing between parallel dislocations and 5a following Weertman and Weertman (30). The quantities K_{11} and K_{33} are complicated functions of the elastic constants c_{ij} and the orientation of the dislocation line. In the isotropic situation K_{11} and K_{33} reduce to $C_{44}/(1-\nu)$ and C_{44} respectively (where ν is Poisson's ratio). Unfortunately, β brass is one of the most anisotropic of all cubic phases and one is forced to make use of the more general forms of K (31,32). The calculations will be performed for binary Cu-Zn equilibrated at 500°C. The pertinent data appear in Table I. Elastic constants are available for β only.

TABLE I

ELASTIC DATA FOR Cu-Zn at 500°C

Quantity	Value	Source
$a^2/\Delta a$	950 Å	Table VI
C_{11}	1.16×10^{12} dynes/cm^2	(33)
C_{12}	1.02×10^{12} "	
C_{44}	0.640×10^{12} "	
S_{11}	4.87×10^{-12} cm^2/dyne	calculated from C_{ij}
S_{12}	-2.28×10^{-12} "	
S_{44}	1.56×10^{-12} "	
at pct Zn in β	48	Hansen (34)
at pct Zn in γ	57	
ν	1/3	assumption

Case I: Isotropic Behaviour

It may be shown that a <100> edge dislocations accommodating misfit in {100} planes. Also, one expects that $\frac{a}{2}$<111> dislocations would appear in {110} planes. For (100),

$$\xi^{100} = C_{44}a^2/10 + \frac{3C_{44}a^2}{8\pi} \ln \frac{\lambda^{100}}{5a} \qquad (2.11)$$

but λ is simply the mismatch distance $a^2/\Delta a$. Evaluating

$$\xi^{100} = 3.33 \times 10^{-4} \text{ ergs/cm}$$

For (110)

$$\xi^{110} = C_{44}a^2/10 + \frac{aC_{44}a^2}{32\pi} \ln \frac{\lambda^{110}}{5a} \qquad (2.12)$$

here λ is $a^2\sqrt{3}/2\Delta a$ or 823Å. Evaluating,

$$\xi^{110} = 2.56 \times 10^{-4} \text{ ergs/cm.}$$

In the case of a grid of dislocations, there will be an interaction energy term when dislocations intersect at less than right angles. Following Hirth and Lothe (35), it may be deduced that the interaction energy is negligible for <111> dislocations intersecting at 70.50° when the spacing is large. For the grid sketched in Figure 5, it is clear that the mechanical energy per unit area is $2\xi/\lambda\sin^2\phi$.

Consequently, the mechanical energy terms for (100) and (110) surfaces are 70.0 and 70.0 ergs respectively. Their equality reflects the assumptions of isotropy.

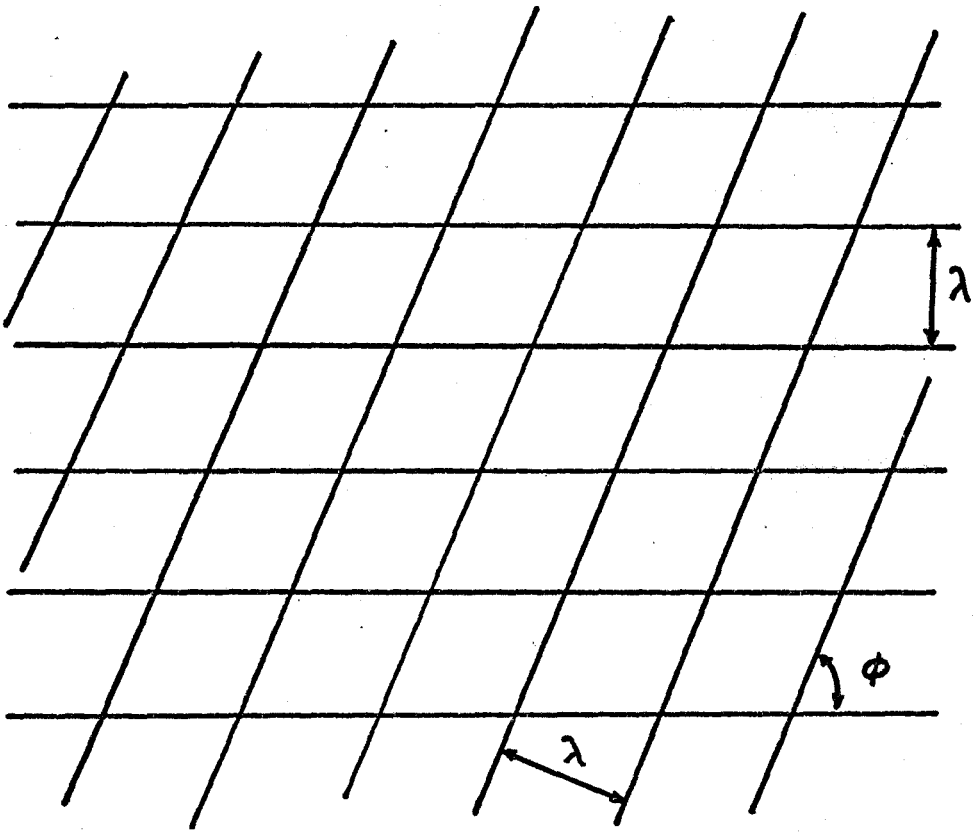

Figure 5. Grid Configuration

Case II: Anisotropic Behaviour

As shown by Eshelby (32) and Foreman (36), an analytic expression for K exists only for a few high-symmetry orientations. Otherwise, a grueling numerical procedure must be followed. Analytic solutions for the two situations of interest have been derived.

Foreman (36) reports that the energy factor for an edge dislocation $a[0\bar{1}\bar{1}]$ lying along [100] in the (001) plane of a cubic crystal is

$$K_{11} = (C_{11} + C_{12}) \left[\frac{C_{44}(C_{11} - C_{12})}{C_{11}(C_{11} + C_{12} + 2C_{44})}\right]^{1/2} \qquad (2.14)$$

which becomes 3.26 x 10" dynes/cm^2 on evaluation. It follows that ξ^{100} is 1.50 x 10^{-4} ergs/cm.

Also, the mechanical energy term is $2\xi/\lambda$ or 31.6 ergs/cm^2.

The net surface free energy of a {100} interface is $\gamma_m + \gamma_c$ or 35.3 ergs/cm^2.

A much more difficult calculation has been performed by Head (29) who supplies the energy factor for an edge dislocation lying in a (110) plane along a $[\bar{1}11]$ direction:

$$K_{11} = \frac{1}{2}\left[\frac{\bar{S}_{11}}{\bar{S}_{44}}(\bar{S}_{11}\bar{S}_{44} - \bar{S}_{15}^2)\right]^{-1/2} \qquad (2.15)$$

in which the $\bar{S}_{ij}$ are functions of the elastic stiffness coefficients S_{ij}. When evaluated, K_{11} is found to be 4.32 x 10" dynes/cm^2. Actually, the dislocation of interest here has Burgers vector $\frac{a}{2}[111]$ and lies along $[11\bar{2}]$; however, there is no analytical solution for this and the case above was selected as an approximation. Taking b equal to $a\sqrt{3}/2$ one obtains a value of 1.45 x 10^{-4} ergs/cm for ξ_{110} indicating that the dislocation chosen

is individually more stable than the a[100] type. However, because less mismatch is relieved by each dislocation, more are required per unit area and it follows that the surface energy is higher. It is, in fact, 39.6 - 2.6 = 37.0 ergs/cm^2. Clearly, for the elastic constants chosen, the model yields unsatisfactory results. Still, considering some of the assumptions made in the calculation the results are numerically quite similar to experimental estimates. The major assumption was that γ brass has the same elastic coefficients as β brass -- a gross assumption but necessary in the absence of any data for γ. Second, it was assumed that the stress fields of interface dislocations behave like those in bulk materials; there is no reason to suppose otherwise. Finally, the approximation to a [111]-type dislocation ignored the energy of the small screw component and all interactions.

The question arises whether the dislocation configuration is determined by the overall surface energy or the individual dislocation energies. The first condition (if the calculation is correct) would lead to equilibrium forms dominated by {100} faces while the second would lead to dodecahedra. Since the latter is actually observed, it is concluded that individual self-energies dominate. This is not surprising since individual dislocations are not seriously affected by macroscopic developments.

Given two cusp orientations one can complete the γ-plot by assuming that all nonsingular interfaces are made up of cusp-facets. Calling ϕ the angle between a nonsingular surface normal and [100], the surface energy at that orientation is

$$\gamma(\phi) = (\gamma_{110}\sqrt{2} - \gamma_{100})\sin\phi + \gamma_{100}\cos\phi \qquad (2.16)$$

Equation (2.16) agrees well in form with that suggested by Shewmon and Robertson (37).

Finally, compare this to the estimate of γ from a van der Merwe network. In this case (38) the misfit dislocation is represented as a continuous "smear" rather than a discrete entity.

Crystals of spacing a and b (with average c) are placed together and a periodic interatomic potential is assigned such that the shear modulus is a parameter. The relative displacements of the atoms gives rise to an increase in potential energy representing the surface energy. In van der Merwe's notation, the result is

$$\tau = \left(\frac{\mu_o C}{4\pi^2}\right) \left[1 + \beta - \sqrt{1+\beta^2} - \beta \ln \left(2\beta \sqrt{1+\beta^2} - 2\beta^2\right)\right] \qquad (2.17)$$

in which

$$\beta = \pi\mu c / p\mu_o(1-\sigma) \qquad (2.18)$$

and $\mu \sim \mu_o$ = shear modulus = 6 x 10" dynes/cm^2

c = spacing at interface = 2.6×10^{-8} cm

p = period of mismatch = 10^{-5} cm , and

σ = Poisson's ratio = 1/3

Equation (2.17) yields 91.6 ergs/cm^2 for a one-dimensional array. For a similar two-dimensional array the surface energy would be 183 ergs/cm^2. Because a potential function was specified, this value includes the chemical term.

Since discrete dislocations have been observed at interfaces by Laird and Aaronson (16), Nicholson and Weatherly (18), Malcolm and Purdy (12), to name a few, the model may not be physically correct but should be energetically correct; in fact, for finite overgrowths the coherency strain is

completely elastic and no dislocations appear until the overgrowth depth reaches a certain value depending on the misfit, and in this case the Frenkel-Kontorova model is the more appropriate.

As a check on the magnitude of γ_{110} the dihedral angles at grain-boundary allotriomorphs was measured as indicated in Figure 6.

When surface energies are anisotropic, the equilibrium condition due to Herring (39) is, for the situation illustrated,

$$\gamma_{12} - \gamma_{10}\cos\theta - \gamma_{20} + \frac{\partial\gamma_{10}}{\partial\theta}\sin\theta = 0 \qquad (2.19)$$

When θ is not near a cusp, the torque term may be neglected. According to Swalin (40), the incoherent interface in brass has a surface energy very nearly equal to the grain boundary energy of about 1000 ergs/cm^2. Measurements by Stephens (41) indicate that θ is about 93^o. Taking γ_{10} to be 50 ergs/cm^2, equation (2.19) yields a value of about 2.5 ergs/cm^2 for γ_{12}-γ_{20} — quite similar to the chemical surface energy γ_c.

A final test was an attempt to correlate the spacing of the experimental perturbations with surface energy. From Sekerka's time-dependent theory (23), the fastest-growing wavelength for large particles is

$$\Lambda_c \approx \sqrt{3} \text{ relative to } \lambda_o \qquad (2.20)$$

Substituting for equation (1.5), the wavelength is

$$\lambda = 2\pi\sqrt{3}\left(\frac{c_o}{C-c_o}\,\Gamma\,\frac{D}{V}\right)^{1/2} \qquad (2.21)$$

The supersaturation estimated from the binary phase diagram on cooling from 500 to 400^{o}C is about 0.01. For the bulk β, D is 10^{-8} cm^2/sec from

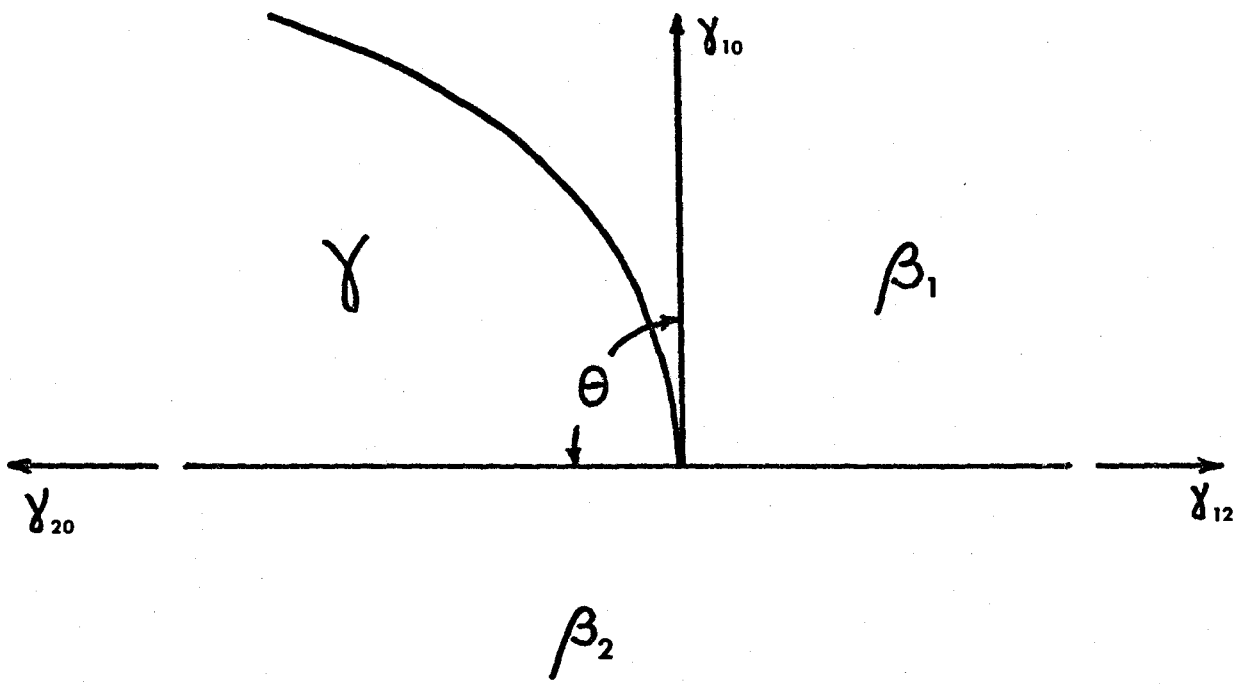

Figure 6. Dihedral Angle Configuration

the data of Landergren et al. (42). The velocity V is estimated as the amplitude of perturbations over the aging time and λ measurements yield values of 10^{-4} cm. Thus the capillarity constant Γ is of order 10^{-6} cm from which γ is of order 100 ergs/cm^2 in good agreement with theory.

CHAPTER 3

EXPERIMENTAL

A series of experiments was undertaken the purpose of which was to compare mobilities as deduced from relative stability with the degree of coherency of the interface.

3.1 Heat Treating

A set of four alloys was prepared by melting together appropriate amounts of 99.999% copper, 99.999% zinc, and 99.99% tin in vycor capsules sealed at a pressure not exceeding 5×10^{-5} mm Hg. The resulting rods, 11 mm in diameter, were hot-rolled to slabs 3 mm thick in two passes. Samples were chemically analysed through the courtesy of the Consolidated Mining and Smelting Company's laboratory and the results appear in Table II .

Specimens of approximately 1×1 cm^2 were cut from the slabs for heat treatment; these were annealed in evacuated vycor tubes at 750^{o}C for 24 hours and furnace cooled to 500 ± 10^{o}C where they were held for between 72 and 100 hours to equilibrate the two phases present. When the equilibration period had elapsed, the specimens were quenched in ice water. After drying, they were placed in a wire basket and immersed in a salt bath composed of 55 wt. pct. KNO_3 and 45 wt. pct. $NaNO_2$ held at 500 ± 5^{o}C for 15 minutes. This step was considered necessary to reverse any changes which may have occurred while the specimens were being quenched, and also, to make possible a more rapid quench from 500^{o}C to the aging temperature.

TABLE II

ANALYSIS OF ALLOY SERIES

Specimen	Cu		Zn		Sn	
	wt. pct.	at pct.	wt. pct.	at pct.	wt. pct.	at pct.
A	49	50	51	50	0.0	0.0
B	49	50	48	48	2.9	1.5
C	51	52	45	45	4.3	2.4
D	56	58	38	38	5.8	3.2

Aging was performed in a similar adjacent salt bath at the temperatures 450, 400 and 350 ± 5°C for 60, 120, and 600 seconds, respectively. This was followed by an ice-water quench.

The purpose of this heat treating procedure was to provide various degrees of supersaturation -- hence various thermodynamic driving forces -- for precipitation of γ. Given that the equilibrium form of a γ crystal is a polyhedron, then the observation of interface breakdown (departure from planarity), serves as an indication of the mobility of the initial interface.

The aged specimens were polished mechanically and electrolytically using a 3:1 methanol-nitric acid solution at -30°C and 6 volts. Formvar replicas were used to prepare carbon replicas (shadowed at 70° with gold-palladium) which were examined and photographed at 80 kV in the Philips EM 300 electron microscope.

Meanwhile, the specimens themselves were examined and photographed in the Zeiss optical metallograph. The photographs appear as Figures 7 through 12.

Several interesting features are at once obvious. On the low magnification photographs -- in particular Figure 8 (d) -- large γ dendrites are evident. These were formed on slow cooling from 750 to 500°C and can grow to very large sizes as some were observed to extend for 2 mm, limited only by the β grain size and impingement.

Also visible are numerous, small precipitate "flowers" -- see Figure 8(b) and 9(b) -- actually dendrites growing with apparent eight-fold symmetry from small precipitates nucleated during the aging process; they were not observed in specimens examined before aging and are in no

On Figures 7 through 12 the letters A, B, C, or D refer to alloys of compositions given in Table II equilibrated at 500°C and quenched and aged at the following temperatures:

7. 450°C	8. 400°C
9. 350°C	10. 450°C
11. 400°C	12. 350°C

250 x

A

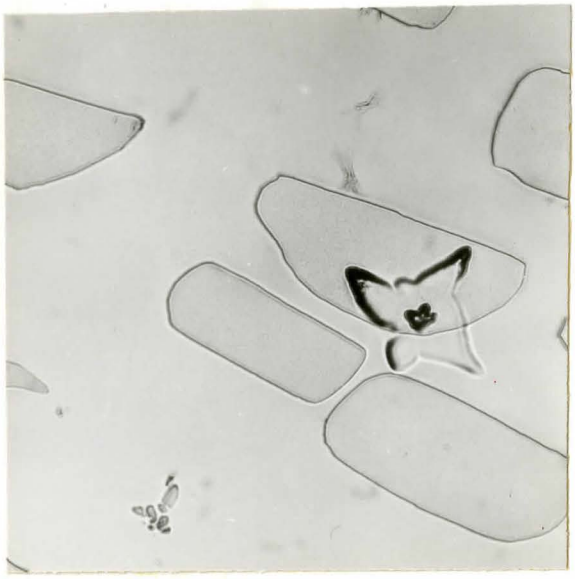

250 x

B

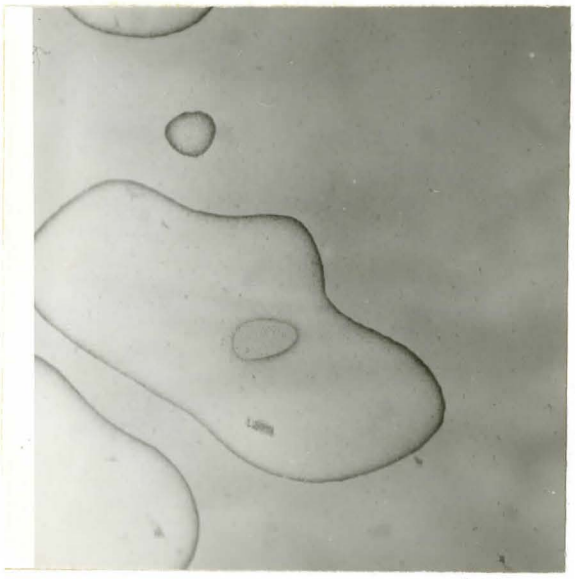

400 x

C

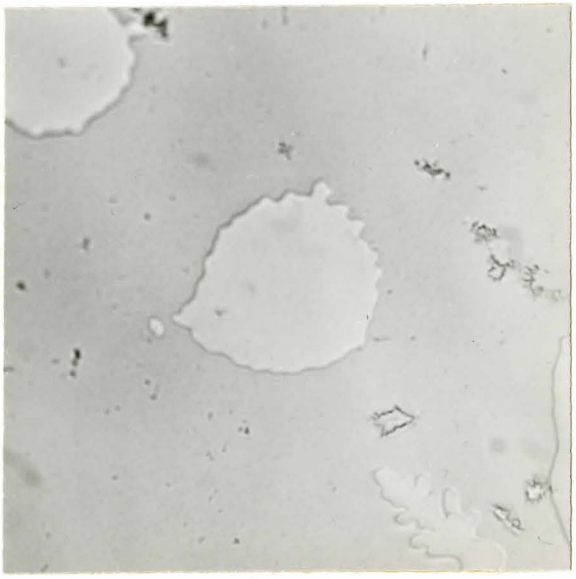

1000 x

D

Figure 7.

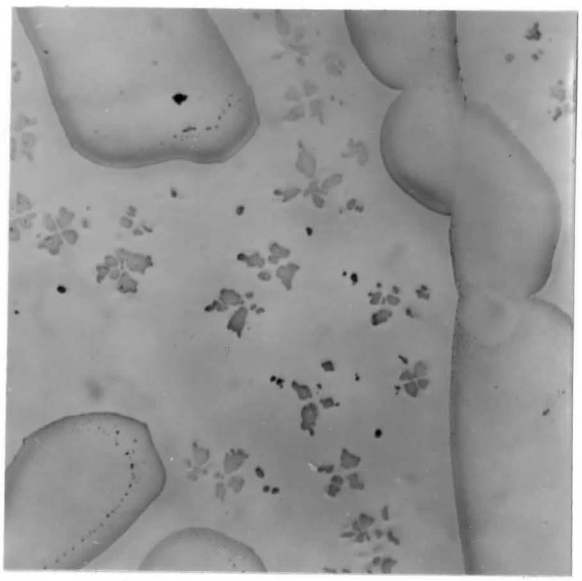

200x

A

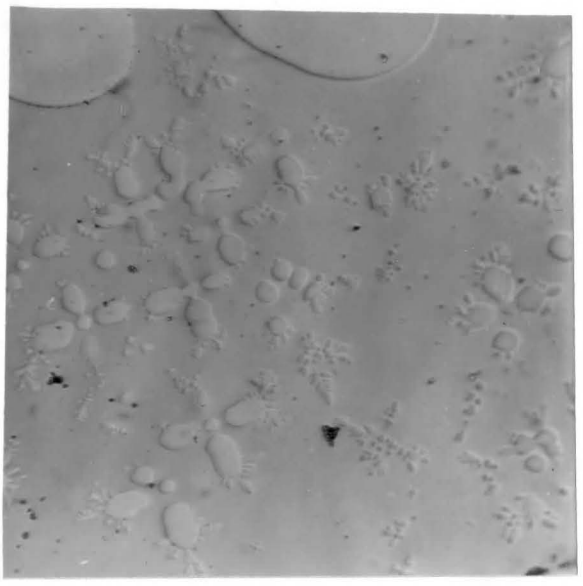

500x

B

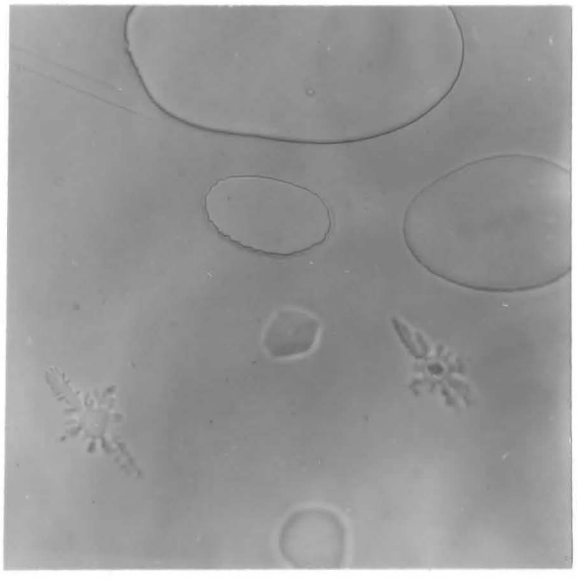

500x

C

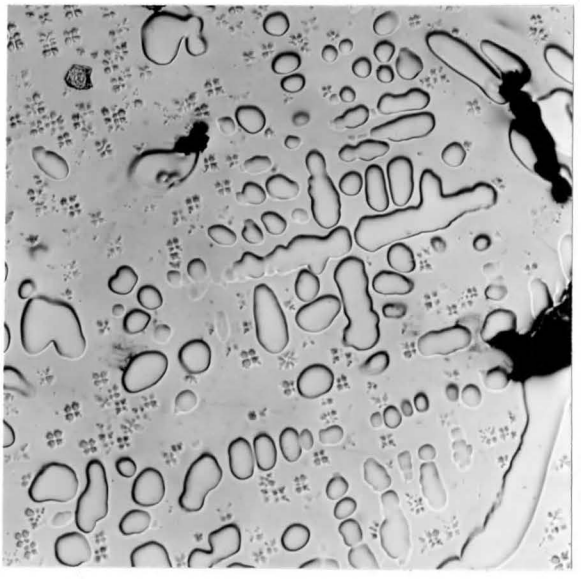

100x

D

Figure 8.

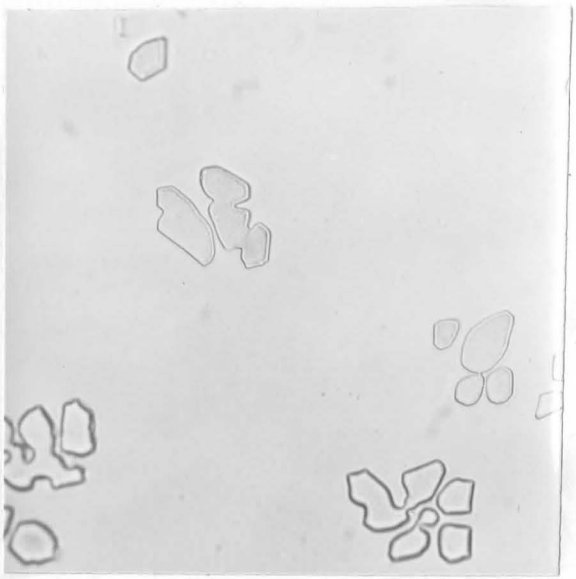

700x

A

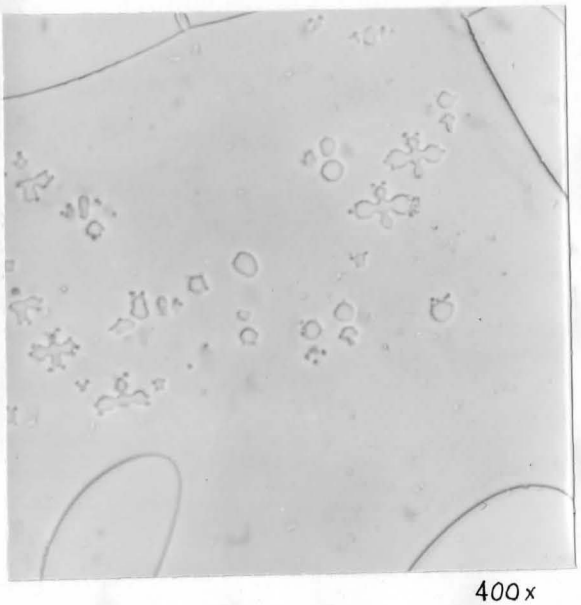

400x

B

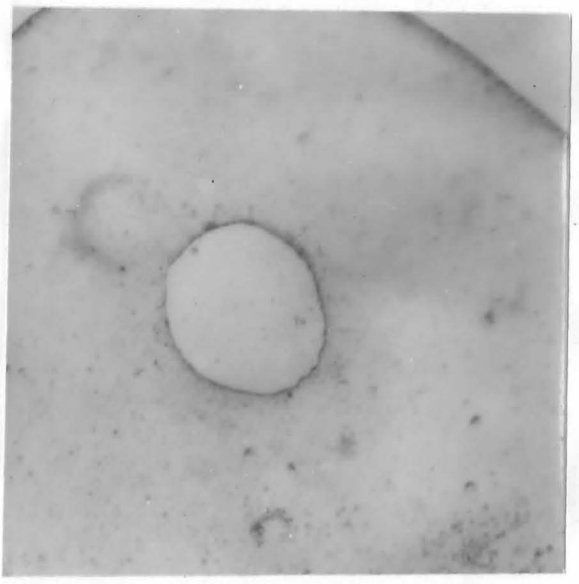

1100x

C

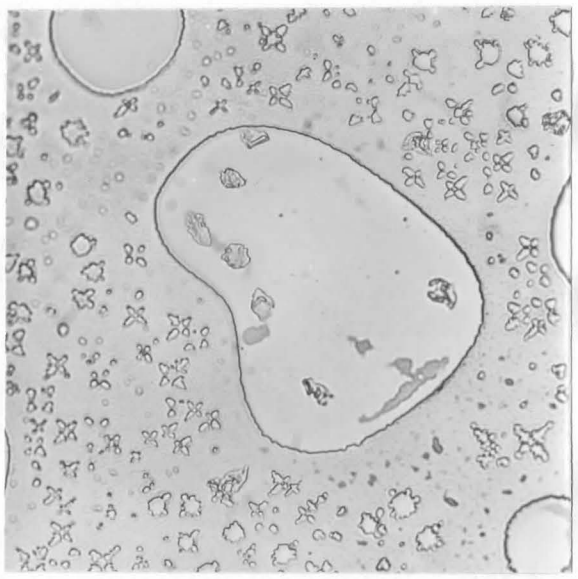

700x

D

Figure 9.

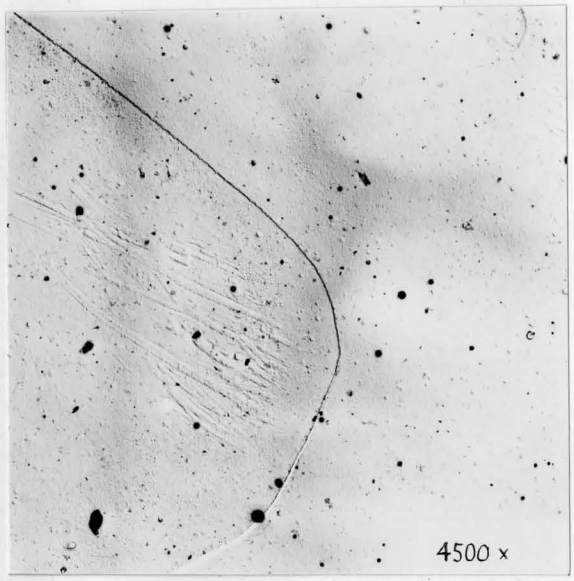

A

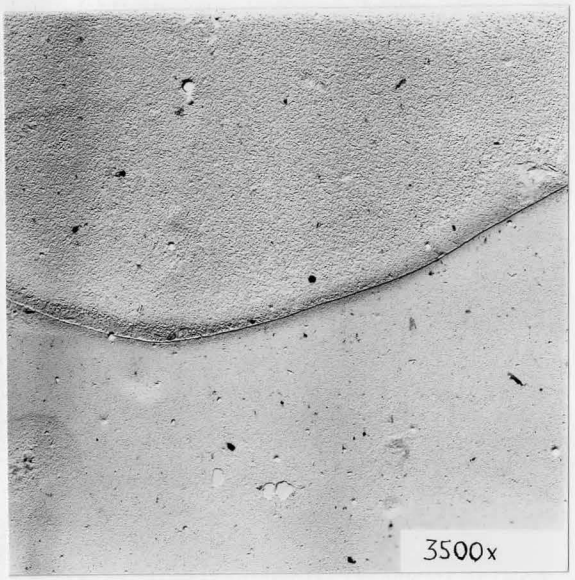

B

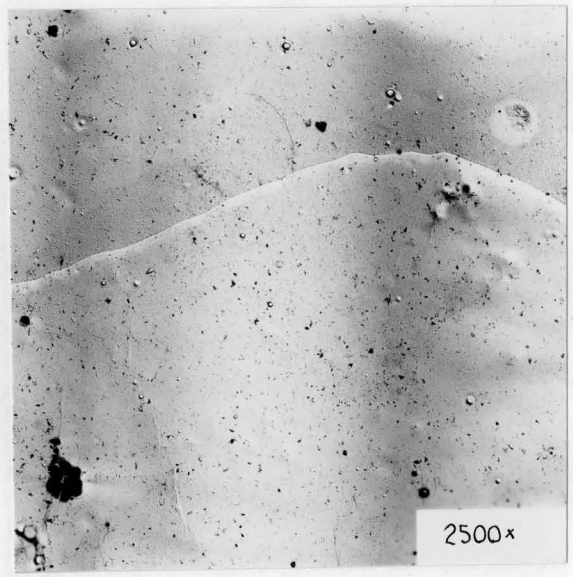

C

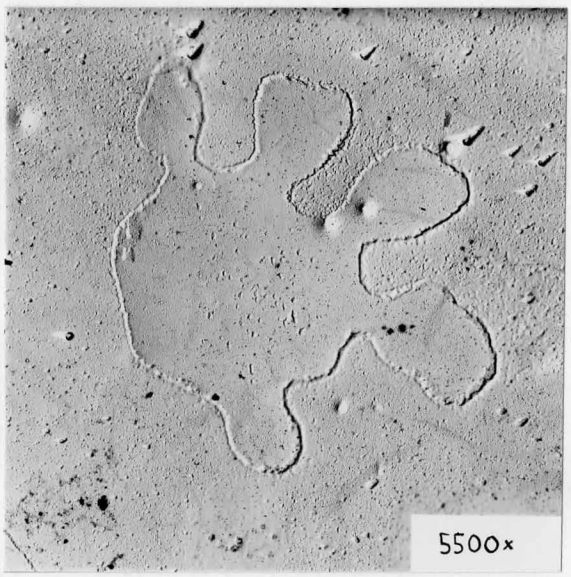

D

Figure 10.

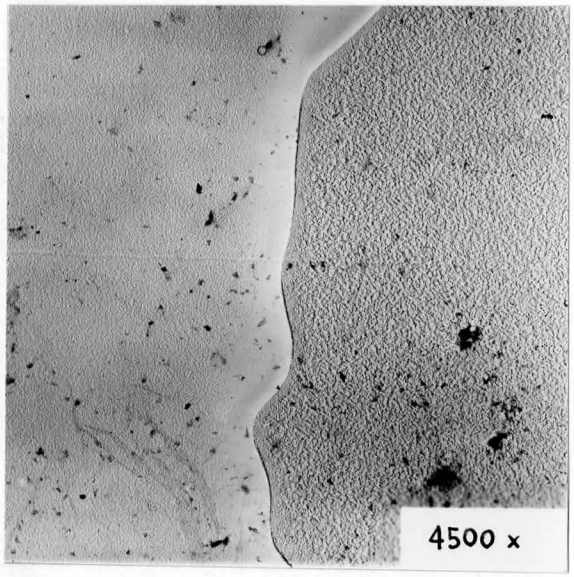

A

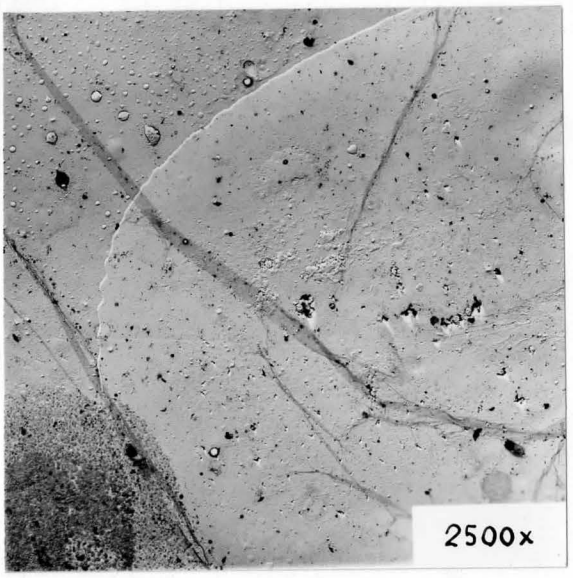

B

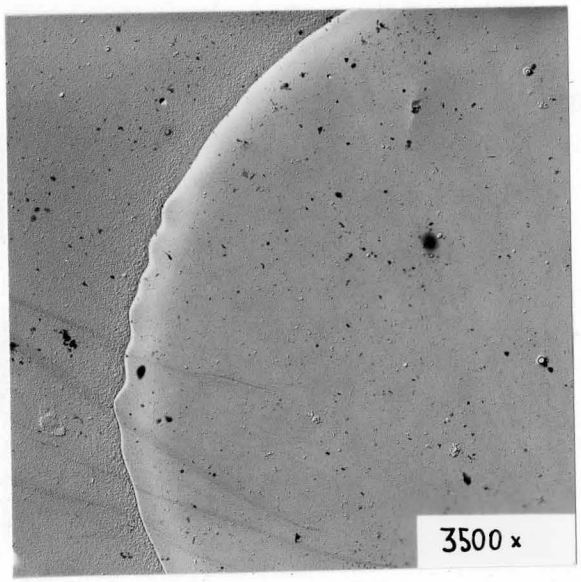

C

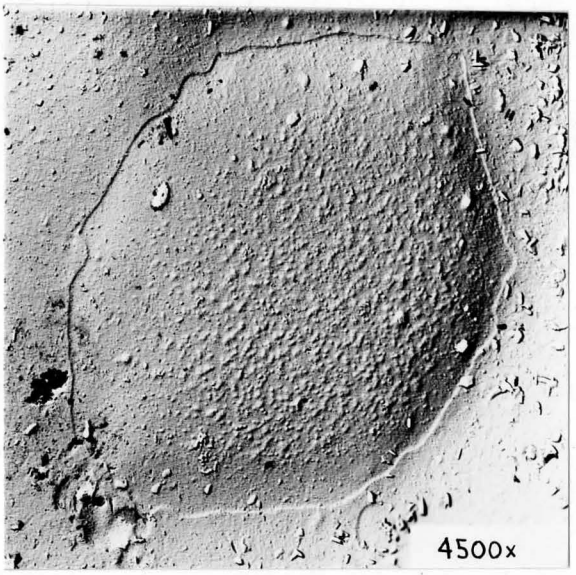

D

Figure 11.

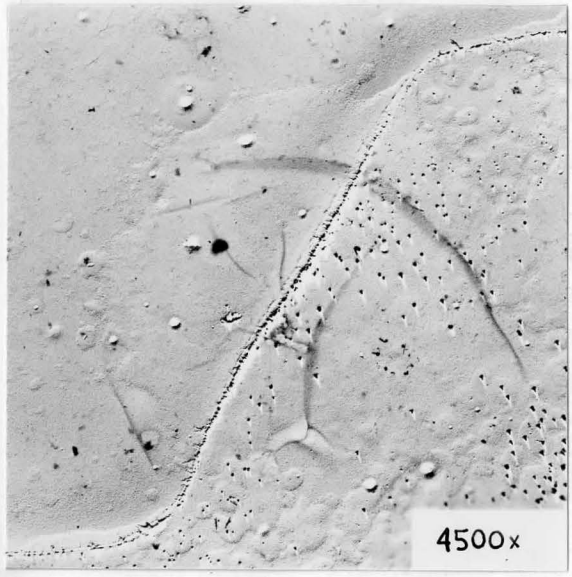

A

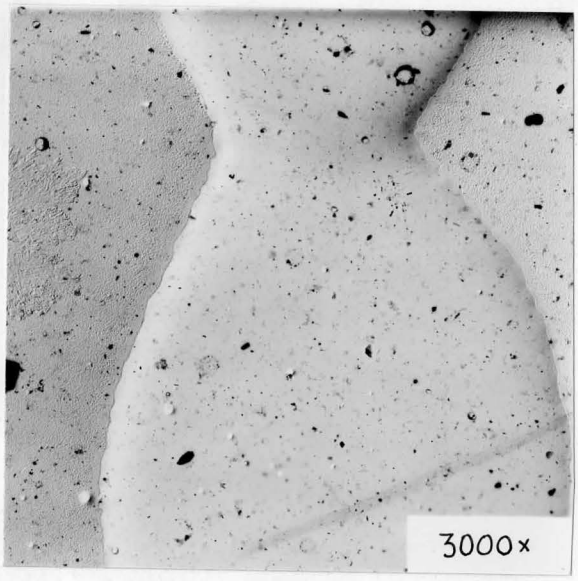

B

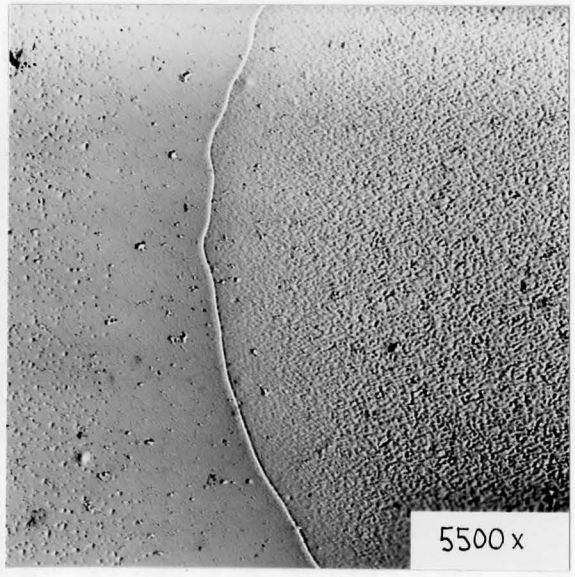

C

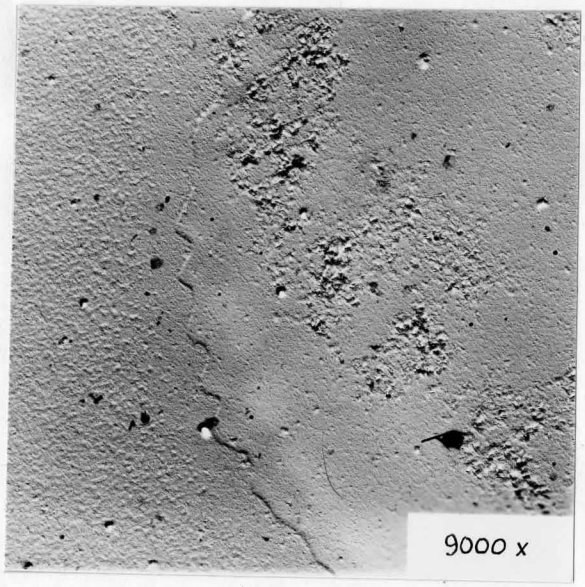

D

Figure 12

instance observed near the large pre-equilibrated γ crystals. Indeed their absence is evidence of a zone near the large crystals which has been depleted of solute.

The third feature visible in some of the electron micrographs is a sinusoidal perturbation of an otherwise smooth interface.

Figures 10(d) and 11(d) appear to represent various degrees in the breakdown of a dodecahedron. The first instabilities appear at edges and grow to large dendrites no doubt due to the greater divergence of the diffusion field near a highly curved particle. But, at a later stage, the faces themselves become unstable as the second picture clearly shows.

Comparing all the photographs one concludes that specimen C was the most easily perturbed followed by D, B, and A.

3.2 The Measurement of Orientations and Lattice Parameters

One of the most elegant and precise methods for determining orientations and lattice parameters is by Kossel microdiffraction (43, 44,45,46). The references should be consulted for full details, but, briefly, the technique consists of bombarding the crystal of interest with a beam of energetic electrons. Inside the crystal, the electrons are decelerated producing x-rays characteristic of the elements present and emitted with spherical symmetry. These divergent x-rays are diffracted from the planes of the crystal yielding cones of diffracted rays and cones deficient because x-rays have been diffracted away from that particular direction (Figure 13).

The pattern recorded on a photographic film is simply a gnomonic projection of cones of semi-apex angle $90^{o}-\Theta_{hkl}$ in which Θ_{hkl} is the Bragg

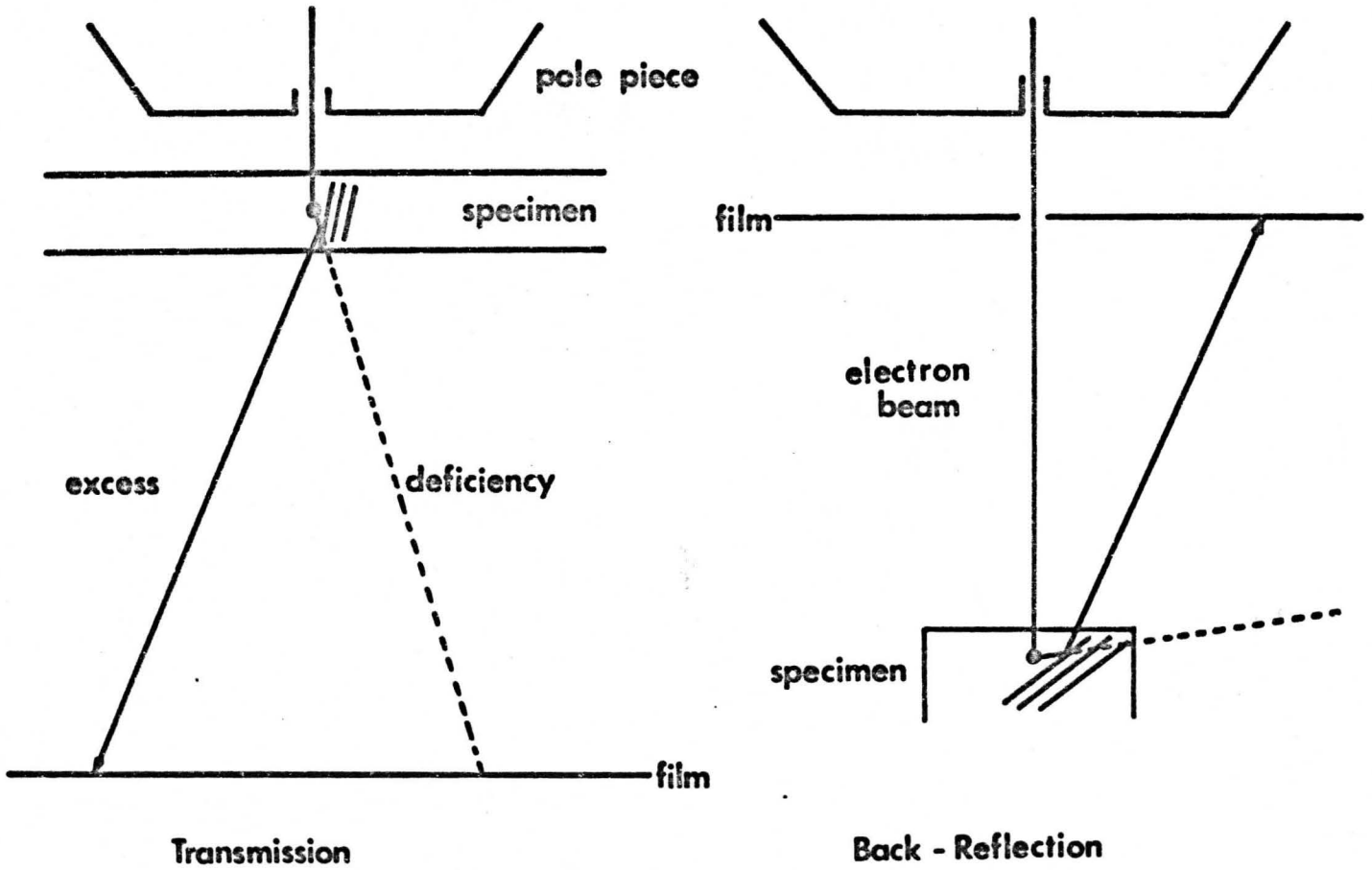

Figure 13. Kossel Modes

angle of the diffracting planes whose normal forms the cone axis. Such patterns are easily indexed by comparison with a previously-prepared gnomonic projection or even a stereogram.

An observable diffraction pattern can only be obtained for crystals of fairly high perfection. If the crystal is too imperfect the diffraction lines may be too diffuse while a too-perfect crystal may yield lines too narrow to be observed. Further, in transmission, the foil thickness should be about $1/\mu$ in thickness (where μ is the appropriate linear absorption coefficient for x-rays). A similar restriction is imposed on the minimum size of crystal which can be analysed: Its diameter should be at least $2/\mu$.

Otherwise, x-rays may be diffracted from neighbouring crystals leading to a superposition of patterns on the film. Finally, when a wavelength different from those normally produced is required, one may place a small amount of a suitable element in close contact with the specimen to act as an emitter. This is known as the pseudo-Kossel technique.

As mentioned earlier, the Kossel technique yields high precision: Within 0.1^{o} in orientation and a few parts per hundred thousand in lattice parameter measurements.

To establish whether grain boundary allotriomorphs grow into the coherent or incoherent grain, a Cu-Zn-Sn specimen was annealed at $700^{o}C$ for 72 hours, furnace cooled to $400^{o}C$ and air cooled to room temperature. The edges were masked in microstop and the specimen was chemically thinned in a solution of 50% acetic, 10% hydrochloric, 30% nitric, and 10% phosphoric acids at $80^{o}C$, until it perforated. The perforation was masked and the specimen was electropolished in a 1:1 phosphoric-water electrolyte at $0^{o}C$ until a second perforation appeared.

The Kossel camera attachment for the Acton microprobe consists of a goniometer with three orthogonal translations, rotation, and tilt along with the appropriate film placement systems. Two major advantages of the transmission mode are apparent: (a) the specimen can be observed through the probe optics and (b) the placement of the film cassette outside the evacuated region allows easier and more rapid film changes. To observe the specimen in back reflection, one must resort to either the backscattered electron image or the specimen current image. In either case they are not very good since the surface is of necessity displaced far beyond the objective lens pole-piece in order to accommodate the film holder. The transmission mode is not as reliable as back reflection for determining the absolute orientations of crystals (47) however, it does yield many more lines and in this experiment only relative orientations are required.

The foil was installed in the camera and diffraction patterns at the crystals labelled β_1, β_2, and γ in Figure 14, were recorded on Kodak Type AA x-ray film. Regretably poor reproductions appear as Figures 15, 16 and 17. Note that the patterns of γ and β_1 are almost identical. Only a few lines in γ correspond to β_2. This indicates that the γ crystal chosen was not so large that x-rays could not escape from it to be diffracted by surrounding β. The possibility arises that <u>all</u> the diffraction may have arisen from β but this is discounted since diffractomer measurements yielded appreciably intense reflections from γ. It is concluded that grain boundary γ grew preferentially into the grain with which it shared a common orientation. More conclusive results obtained by Stephens (41) bore this out.

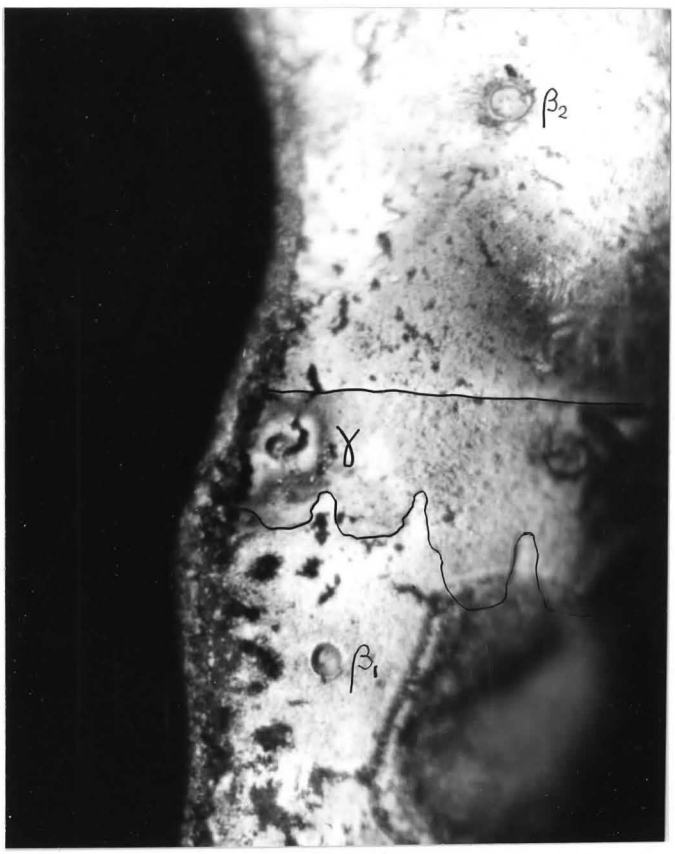

Figure 14. Kossel Specimen 500×

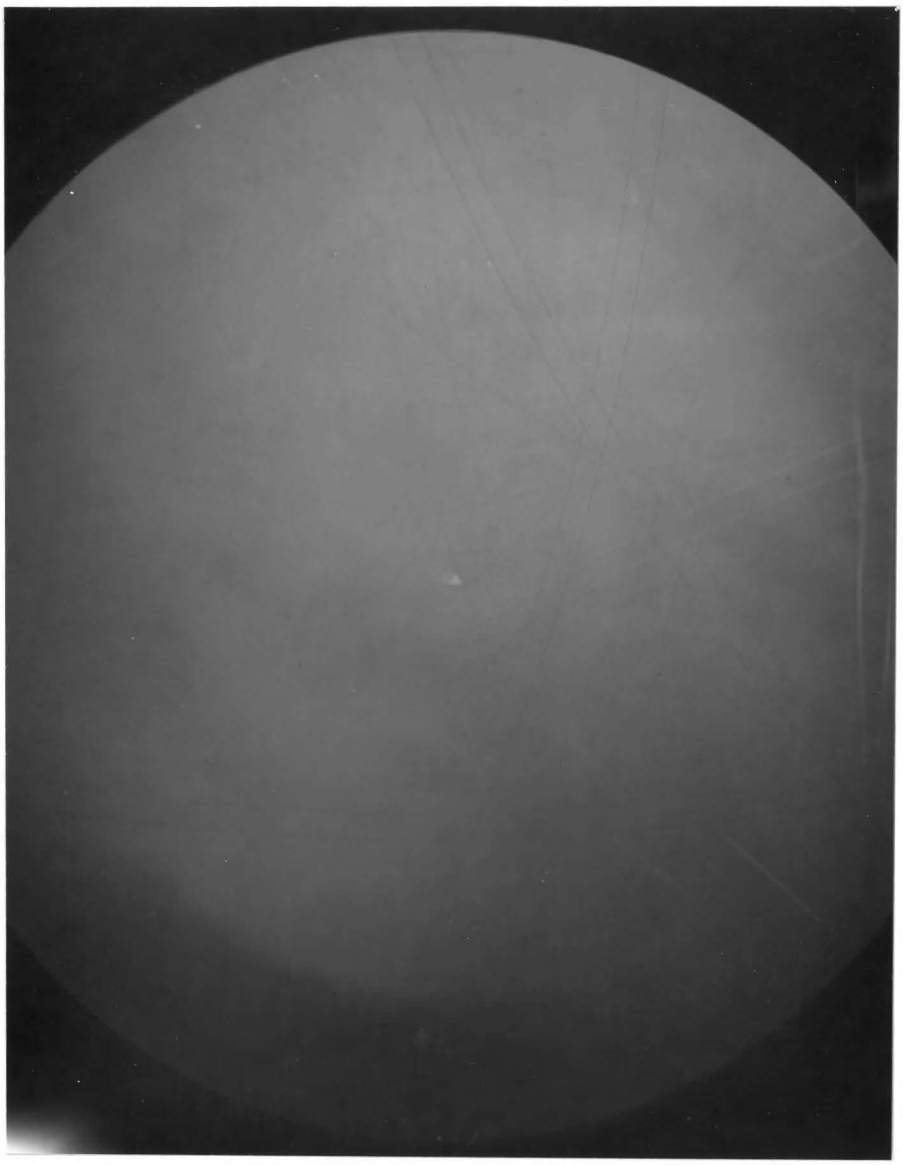

Figure 15. Pattern from β_1

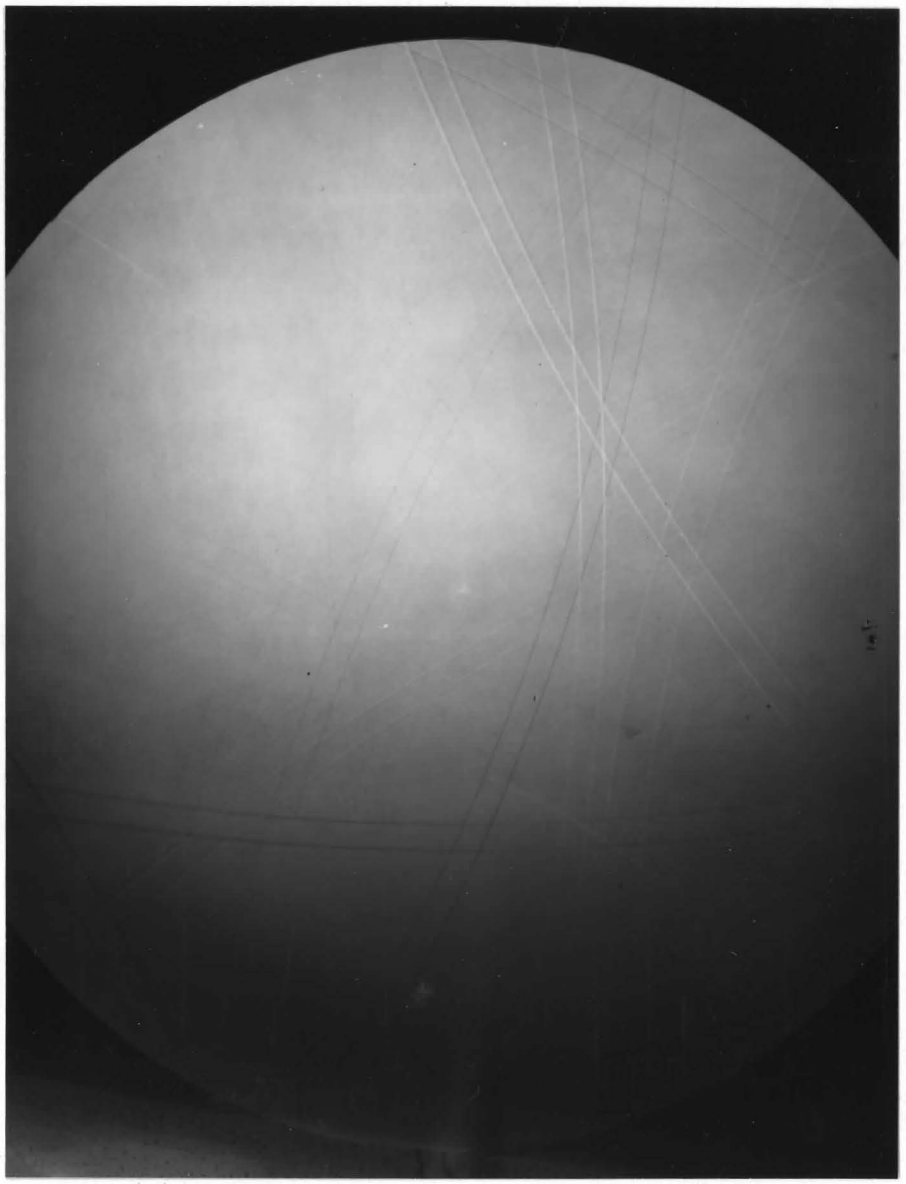

Figure 16. Pattern from γ

Figure 17. Pattern from β_2

An attempt was made to obtain precise lattice parameters from transmission Kossel photographs but no suitable pattern could be obtained for γ brass. The method is reviewed in Appendix I. Finally, a modified powder method was adopted.

Specimens of the hot-rolled Cu-Zn-Sn stock proved to be unsuitable for examination because they yielded rather broad diffraction maxima. Consequently, the well-annealed specimens which had been aged for a few seconds at 450°C were used. These were lightly repolished and mounted in the rotating specimen holder along with a standard of 99.9% nickel. Nickel-filtered copper radiation was used and scans were made at $\frac{1}{2}$ degree 2θ per minute. The results are sketched in Figure 18 for specimens A, B, C, D and a standard of 99.999% copper.

One immediately observed that the γ_{330} peak moves nearer the β_{110} peak on going from A to D and eventually merges into it. This qualitatively indicates that the lattice mismatch approaches zero as tin is added to the system.

The quantitative results were obtained as follows: taking the lattice parameter of the pure nickel standard as $3.52606_{\pm 2}$ Å after Hanneman et al.(48), the Bragg angles for nickel reflections were calculated using the wavelength of CuKα radiation corrected for refraction in nickel (see Appendix II). By measuring the chart distance between the Ni 111 and 200 reflections, it is possible to calibrate the chart against true angular separation. Then by measuring the chart distance between a nickel reflection and a brass reflection, and converting it to an angle, it is possible to determine the Bragg Angle -- hence the lattice parameter -- of the brass much more precisely than is normally possible. The data employed

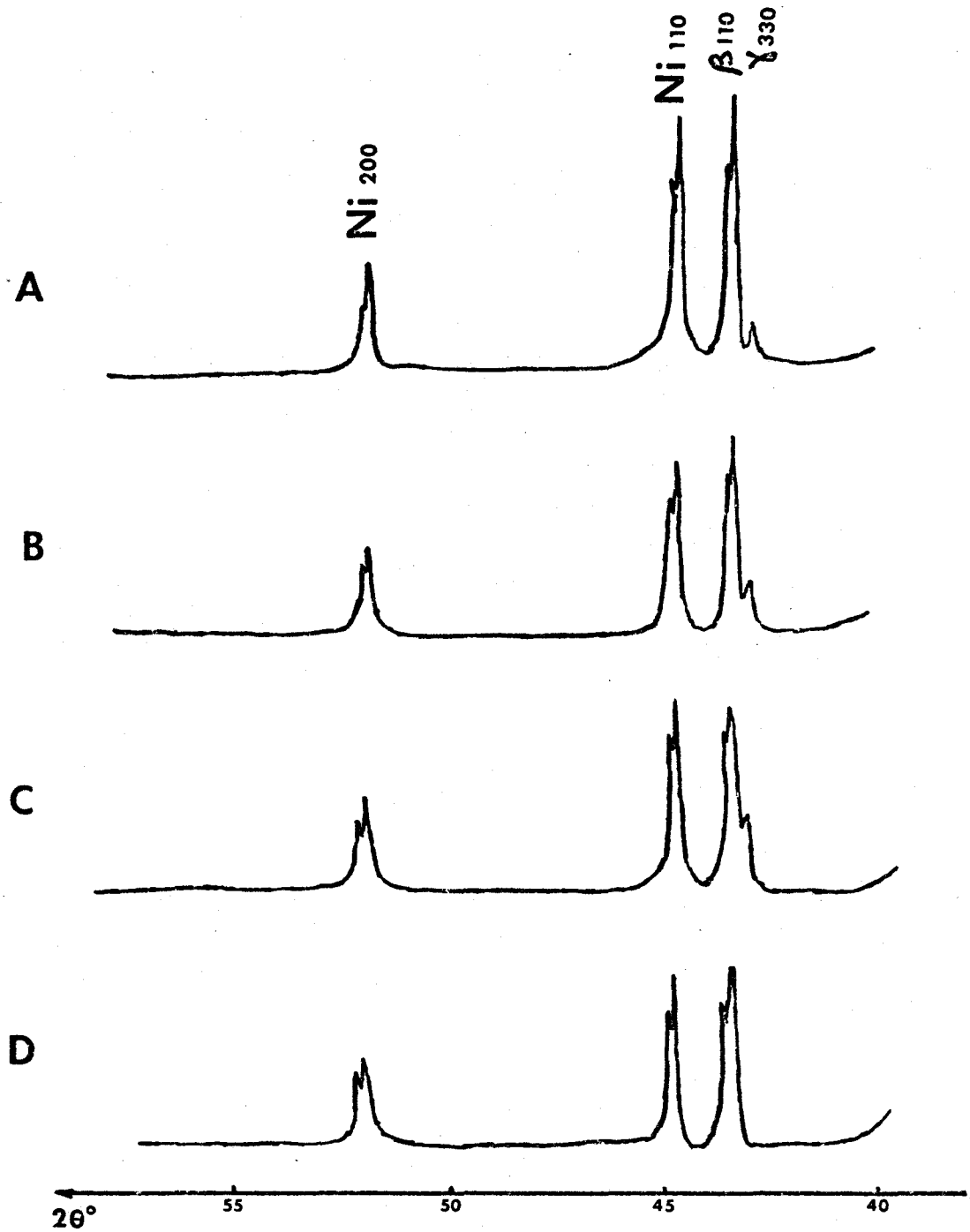

Figure 18. Diffractometer Results

are listed on the following page along with their sources.

It should be noted that throughout the analysis, diffraction maxima rather than centroids were used. For narrow diffraction lines, the difference is negligible. The results appear in Table IV in which $\frac{1}{3} a_\gamma$ has been reported.

It is observed that the lattice parameters of β and γ Cu-Zn do not agree with the data published in Pearson's book (50) for phase compositions corresponding to the 500°C phase boundaries. The results for the copper standard are in excellent agreement with the value of 3.6147Å published in Barrett and Massalski (49) suggesting that the units in Pearson should perhaps be Å rather than kX and vice versa for γ

In what follows, the misfit refers to the difference $\frac{1}{3} a_o^\gamma - a_o^\beta$ since one unit cell of γ closely resembles 27 unit cells of β. Apparently, the lattice misfit passes through zero for some composition between C and D. In Table V are presented the mismatches Δa along with $\lambda = a^2/\Delta a$.

3.3 A Phase Diagram Investigation

In order to estimate the degree of supersaturation produced on quenching from 500°C to lower temperatures, the $\beta + \gamma$ region of the Cu-Zn-Sn system was investigated.

Specimens were sealed in evacuated vycor capsules, homogenized at 750°C for 24 hours and then furnace cooled to either 500 or 400°C and held for 48 hours to equilibrate the system. After being quenched in ice water, the specimens were mounted along with high purity standards of copper, zinc, and tin and were polished mechanically through 0.5 micron alumina but were not etched. Measurement of CuKα and SnLα intensities

TABLE III

Quantity	Value(Å)	Comments	Source
a_o of Ni	$3.52606_{\pm 2}$	trans. Kossel analysis	Hanneman et al (48)
λ of $CuK\alpha_1$ in vacuo	$1.540562_{\pm 5}$	as of 1965	Barrett and Massalski (49)
in Ni	$1.540520_{\pm 5}$	corrected for refraction	
in β brass	$1.540526_{\pm 5}$		
in γ brass	$1.540526_{\pm 5}$		

TABLE IV

DIFFRACTION RESULTS

Specimen	Lines	Distance(mm)	$\Delta 2\theta^{o}$	θ^{o}	Parameter($\mathring{A}$)
A	β110-Ni111	34.2	$1^{o}2.34'$	$21^{o}42.76'$	2.9444_{6}
	γ330-Ni111	39.4	$1^{o}10.98'$	$21^{o}38.44'$	2.9537_{5}
B	β200-Ni200	370.0	$11^{o}11.4'$	$31^{o}30.08'$	2.9482_{6}
	γ332-Ni111	120.1	$3^{o}28.10'$	$24^{o}2.98'$	2.9550_{7}
C	β110-Ni111	39.1	$1^{o}10.68'$	$21^{o}38.59'$	2.9534_{0}
	γ330-Ni111	40.9	$1^{o}13.92'$	$21^{o}36.97'$	2.9569_{3}
D	β211-Ni220	95.0	$2^{o}51.18'$	$39^{o}35.20'$	2.9607_{0}
	γ510-Ni200	23.8	$0^{o}42.90'$	$26^{o}15.83'$	2.9586_{2}
Cu	Cu111-Ni111	38.2	$1^{o}8.58'$	$21^{o}39.64'$	3.6144_{6}

TABLE V

Specimen	$\Delta a(\mathring{A})$	$\lambda(\mathring{A})$
A	0.0094	950
B	0.0069	1300
C	0.0024	3730
D	-0.0015	5960

was carried out in the Acton microprobe under the following conditions: 25kV; 200 na specimen current on copper; 18^{o} takeoff angle; 3 micron spot size; and 10 second counting time.

To convert from the intensity of A in the alloy relative to that of pure A to the weight fraction C_A of A in the alloy, use was made of the standard absorption and atomic number corrections. For a series of compositions, the corrected intensity ratios were calculated and the interpolation formulae for the results were

$$C_{Cu} = 1.01\ I_{Cu}/I_{(cu)}$$

$$C_{Zn} = 1.01\ I_{Zn}/I_{(Zn)}$$

$$C_{Sn} = 1.34\ I_{Sn}/I_{(Sn)}$$

The $500^{o}C$ set yielded results in which the measured zinc content of both phases in the binary was about 4 wt. pct. too high. Therefore, all the results were standardized by subtracting 4 wt. pct. Zn. The tin measurements were correct as above. (This procedure was verified through the use of ternary standards).

Results from the $400^{o}C$ set were consistent for β but were widely scattered for γ suggesting that due to the low diffusivity of elements in γ, the large precipitates had not attained equilibrium in the 48-hour period. Assuming the β compositions were correct, ternary tie-lines were constructed using the lever rule and statistical estimates of volume fractions obtained by superposing a square grid on the microstructures and counting the number of nodes lying over precipitates.

TABLE VI

MICROPROBE RESULTS

T°C	Specimen		$100I_{Sn}/I_{(Sn)}$	$100C_{Sn}$	pct.Sn	$I_{Cu}/I_{(Cu)}$	C_{Cu}	pct.Cu	IZn/I(Zn)	C_{Zn}	pct.Zn
500	A	β:	0	0	0	0.465	0.470	51.0			49.0
		γ:	0	0	0	0.402	0.406	44.6			55.4
	B		1.08	1.4	1.4	0.429	0.433	47.3			39.4
			4.78	6.4	6.4	0.449	0.453	49.3			41.3
	C		1.66	2.2	2.2	0.497	0.502	54.2			43.6
			8.97	12.0	12.0	0.411	0.415	45.5			42.5
	D		2.26	3.0	3.0	0.594	0.600	64.0			23.0
			10.2	13.5	13.5	0.592	0.598	63.8			22.7

continued ...

TABLE VI

MICROPROBE RESULTS

T°C	Specimen		$100I_{Sn}/I_{(Sn)}$	$100C_{Sn}$	pct.Sn	$I_{Cu}/I_{(Cu)}$	C_{Cu}	pct.Cu	$IZn/I(Zn)$	C_{Zn}	pct.Zn
400	A	β:	0	0	0				0.541	0.546	50.6
		γ:	0	0	0				0.613	0.619	47.9
	B		1.94	2.6	2.6				0.490	0.495	45.5
			11.1	14.9	14.9				0.457	0.462	44.2
	C		1.94	2.6	2.6				0.481	0.486	44.6
			10.9	14.6	14.6				0.450	0.455	41.5
	D		2.4	3.2	3.2				0.453	0.448	40.8
			11.8	15.8	15.8				0.427	0.431	39.1

The measured intensity ratios, calculated Cj, and corrected wt. pct. i appear in Table VI.

The phase diagram isotherms estimated from these data and quantitative metallography appear as Figure 19(a) and (b). The limits of error are estimated (for the β phase) at ± 2 pct. Zn and ± 0.5 pct. Sn. It is observed that the phase boundaries do not move significantly in 100°C of cooling. The upper limit of supersaturation is therefore 2/50.

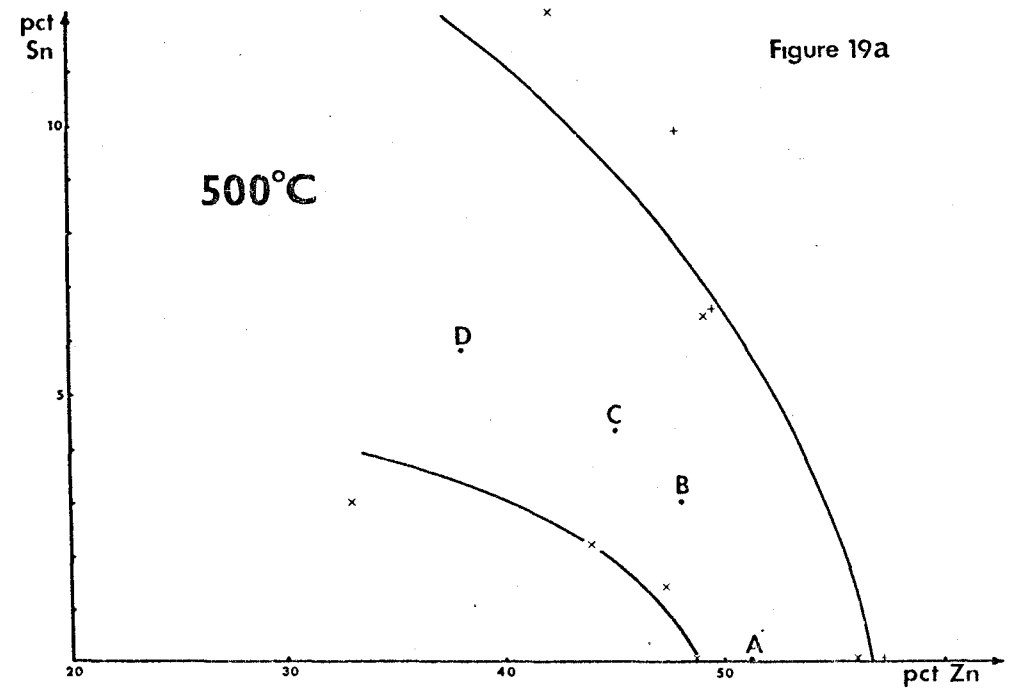

Figure 19a

× probe result
+ lever rule result

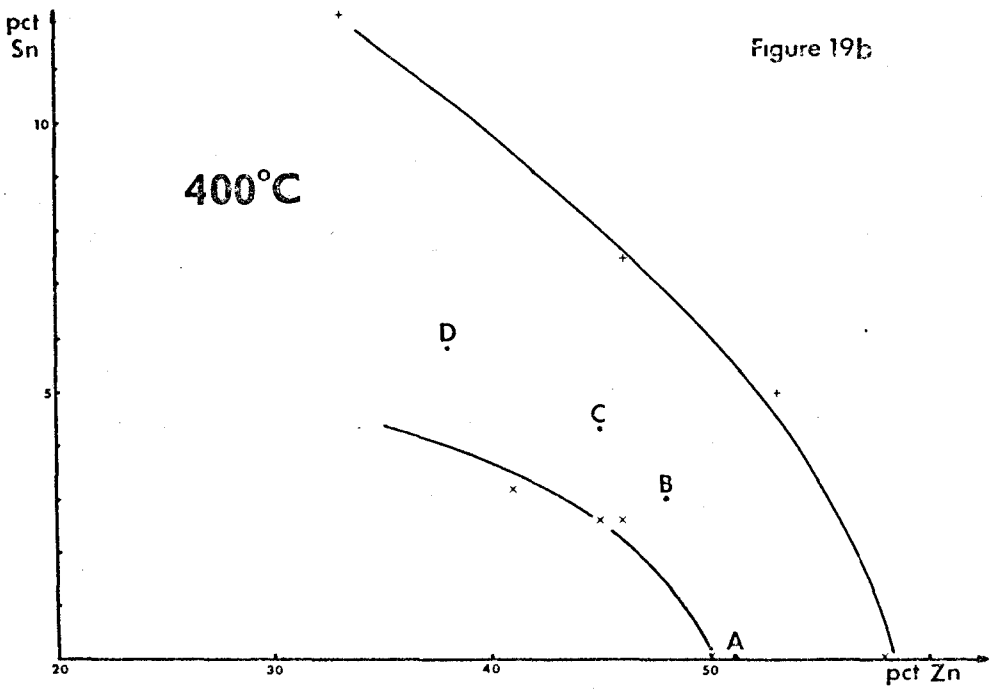

Figure 19b

CHAPTER 4

KINETIC PROPERTIES OF SEMI-COHERENT INTERFACES

In most discussions of transformation kinetics, the influence of volume change is neglected. However, unless the strains of transformation are relieved at a sufficiently rapid rate, the pressure generated can modify the local equilibrium in such a way that the rate of transformation is reduced. Thus, it is not always wise to assume the transformation is isobaric unless, of course, one of the external phases happens to be a fluid.

The purpose of what follows is to estimate the volume strain, to comment on the feasibility of a few relaxation mechanisms, and to speculate as to the effect of strain on growth morphologies.

4.1 Volume Change of Transformation

Consider a system of N atoms occupying a volume V and having a structure with n atoms per unit cell of volume u. This transforms isothermally to two (stress-free) phases containing N' and N" atoms in volumes V' and V" and having structures specified by n', u' and n" and u". Conservation of atoms requires

$$N \equiv N' + N'' \tag{4.1}$$

Alternatively,

$$\frac{n'V'}{u'} + \frac{n''V''}{u''} = \frac{nV}{u} \tag{4.2}$$

Following Darken and Gurry (51), an equilibrium relation between N' and N" is

$$N'd'' = N''d' \tag{4.3}$$

in which d' and d" are equal to x-x' and x"-x where the x's are equilibrium phase boundary compositions in atom fractions for a binary system. For a C-component system, these quantities become

$$d' = \left(\sum_{i=1}^{C} (x_i - x_i')^2\right)^{1/2} \tag{4.4}$$

and

$$d'' = \left(\sum_{i=1}^{i} (x_i'' - x_i)^2\right)^{1/2}$$

It is possible to solve (4.2) for V' and V" in terms of V. The solutions are

$$V' = V\left[\frac{nu'}{n'u}\left(\frac{d'}{d' + d''}\right)\right] \tag{4.5}$$

and

$$V'' = V\left[\frac{nu''}{n''u}\left(\frac{d''}{d' + d''}\right)\right]$$

Assuming that compositions and atomic volumes are constrained to the above values, the total volume strain is (V' + V" - V)/V or

$$\frac{n}{u(d' + d'')}\left[\frac{d'u'}{n'} + \frac{d''u''}{n''} - \frac{(d' + d'')u}{n}\right] \tag{4.6}$$

This represents the maximum, unrelieved volume strain at the completion of decomposition.

A kinetic approach to the same problem is as follows. A spherical particle of radius R and homogeneous composition $\{C_i''\}$ growing at velocity ν into a matrix of bulk composition $\{C_i'\}$ satisfies the diffusional mass balance:

$$\nu\,(C_i'' - C_i') = -\,J_i(R) \qquad (4.7)$$

In (4.7) $J_i(R)$ is the flux of species i at the interface and the compositions are measured in atoms per unit volume. Sum equation (4.7) over all C components and recognize that the sum of all c_i'' is $1/\Omega''$ -- the total number of atomic species per unit volume of precipitate -- and the sum of all c_i' is $1/\Omega'$, and also, the sum of all $-J_i(R)$ is exactly the Kirkendall vacancy flux at the interface:

$$J_o(R) = \nu\left(\frac{1}{\Omega''} - \frac{1}{\Omega'}\right) \qquad (4.8)$$

Let $dV = VAdt$ be the volume of matrix of composition C_i^∞ and atomic volume Ω^∞ which transforms to an equal -- but stressed -- volume of precipitate of composition c_i''' and atomic volume Ω''' at an interface of area A in a time interval dt. The number of atoms in this volume is dV/Ω^∞. Stress-free precipitate containing this many atoms would occupy a volume $dV_o = \Omega'' dV/\Omega^\infty$. The maximum volume change is

$$\left(\frac{\Omega''}{\Omega^\infty} - 1\right) dV \qquad (4.9)$$

Yet, the Kirkendall flux may act so as to relieve this strain since

$$J_o A dt = \nu A dt\left(\frac{1}{\Omega'''} - \frac{1}{\Omega'}\right) \qquad (4.10)$$

is the number of vacancies moving away from the precipitate. At the external surface, the volume associated with this many vacancies is

$$\Omega^\infty\,\nu A dt\left(\frac{1}{\Omega'''} - \frac{1}{\Omega'}\right) = \left(\frac{\Omega^\infty}{\Omega'''} - \frac{\Omega^\infty}{\Omega'}\right) dV \qquad (4.11)$$

Thus, the actual volume difference, including the above effect is

$$\left(\frac{\Omega''}{\Omega^\infty} - 1\right) dV + \left(\frac{\Omega^\infty}{\Omega'''} - \frac{\Omega^\infty}{\Omega'}\right) dV \qquad (4.12)$$

Assuming all deformation occurs in the softer matrix, one may set $\Omega''=\Omega'''$. It is safe to assume that Ω^{∞} refers to unstressed bulk matrix and Ω' to stressed matrix at phase boundary composition.

In the case of Cu-Zn-Sn, $\Omega'' > \Omega^{\infty} > \Omega'$ so that the first term in (4.12) is positive while the Kirkendall effect term is negative and acts to relieve the volume strains.

A more complete analysis requires a pressure-composition linkage such as Li and Blakely (52) have undertaken for steady-state processes such as Ostwald ripening.

The preceding argument can be modified to include fluxes due to stress gradients by writing Fick's first law in the form:

$$\underline{J_i} = - D_i[\nabla c_i + \frac{c_i(\Omega_i - \Omega)}{kT} \nabla p] \qquad (4.13)$$

where $(\Omega_i - \Omega)$ is the volume change of replacing an "average" atom with one of species i in the hydrostatic pressure field p. For spherical symmetry, Mott and Nabarro (52) have shown p(r) to be:

$$p(r) = \frac{2}{3} \frac{(1 - \nu)}{(1 - 2\nu)} \frac{eER^3}{r^3} \qquad (4.14)$$

in which E and ν are Young's modulus and Poisson's ratio for the matrix, and e is a measure of the elastic strain at the (coherent) interface given by $\frac{3K\delta}{3K + 2E/(1 + \nu)}$ for misfit δ and precipitate compressibility, K. Thus equation (4.13) can be put into the form

$$J_i = - D_i \{ \frac{\partial c_i}{\partial r} - \frac{\beta_i c_i}{r^4} \} \qquad (4.15)$$

Writing Fick's second law for constant D_i leads to a partial differential equation with solution $C_i(r,t)$. Without solving for $C_i(r,t)$ one can appreciate the effect of the form of (4.15) on the preceding argument. The pressure-volume term leads to an enhancement of the vacancy flux which tends to relieve strains near the precipitate. This is satisfactory since the final state must be strain-free precipitate and matrix.

However, such a relaxation mechanism requires sources capable of producing prodigious quantities of vacancies. In a fairly perfect, coarse-grained matrix, the absence of such sources as grain boundaries and external surfaces could limit the vacancy flux to a value insufficient for relaxation. (Sources of vacancies are considered in the next section). The strain energy generated in the absence of a vacancy flux would be of the form suggested by Nabarro (54), namely $K'V^*(\Delta V/V)^{1/3}$, (4.16) where K' is the matrix compressibility and all the strains are assumed to be in a volume V* of the matrix.

When particles are small, or have a small radius of curvature, it is possible that prismatic dislocation loops could be punched. Recently, two criteria for loop-punching have been suggested. Weatherly (55) proposes that a loop can be punched when the resolved shear stress on the prismatic slip plane exceeds the theoretical shear strength $\mu/30$. For ellipsoids in pure dilatation, the resolved shear stress on the (111) fcc slip plane is about $\frac{2}{3}\,\mu\,\Delta V/V$.

A similar computation carried out for (110) planes in bcc yields a value of about $\frac{3}{4}\,\mu\,\Delta V/V$. Hence, the volume strain required for loop-punching is about 0.04.

The other criterion, due to Brown and Woolhouse (56), is based on the total loop energy: the self energy E(self) plus the energy E(int) of interaction of the loop with the particle stress field. Using Mott and Nabarro's strain field for a sphere in an isotropic matrix, they obtained a critical loop radius R_c, expressed in terms of core radius r_c and constrained relative misfit e as

$$R_c = \frac{b}{16\pi e(1-\nu)} \left[\ln 8R_c/r_c + \frac{3-2\nu}{4(1-\nu)}\right] \qquad (4.17)$$

such that when the loop lies in the interface, the total loop energy decreases for $R > R_c$ favouring growth.

Using the data in Table VII , the quantities R_c and $\Delta V/V$ are calculated. The very low value of R_c indicates that loop punching is always energetically favoured and the value of $\Delta V/V$ is comparable to the value required for loop punching. Still, Brown and Woolhouse neglect the presence of any loop nucleation barrier which would prevent loop punching at larger particle sizes.

The loop-punching phenomenon has been observed by Jones and Mitchell (57) who generated strains through the thermal contraction of glass spheres in AgCl. Also, Eikum and Thomas (58) observed loops with Burgers vector $\frac{a}{2}[101]$ being punched in Al-Mg_2Si the precipitate grew. Some of the loops they observed had diameters of about 0.5 micron indicating that even large loops can be generated.

Since the loops energy contains the elastic parameter, K, certain loop configurations require less energy than others in keeping with the anisotropic nature of solids. It was found in the chapter on static

TABLE VII

$b = a\sqrt{3}/2 = 2.55 \times 10^{-8}$ cm

$d' = 0.3$

$d'' = 0.7$

$n = n' = 2 \quad ; \quad n'' = 52$

$u = (2.953 \times 10^{-8})^3$ cm^3

$u' = (2.944 \times 10^{-8})^3$ cm^3

$u'' = 27(2.955 \times 10^{-8})^3$ cm^3

$\therefore \Delta V/V = 0.026$

$\nu = 1/3$

$r_c = 5a = 1.5 \times 10^{-7}$ cm

$e = 0.004$

$\therefore \quad R_c \simeq 0.8\text{Å}$

properties that the line energy ξ of a dislocation in β brass is a minimum for dislocations of the type $\frac{a}{2}$ <111> . Therefore, it is possible that loops could be punched in all eight <111> directions about a small sphere of γ. If such loops, upon relieving the local pressures, led to the generation of stable perturbations, it could explain the peculiar "flower" morphology observed in Figures 8(b) and 9(b). However, there is, at this time, no visual evidence of loops near γ particles although there is no evidence of their absence either.

In the case of very large spheres, or a planar interface, loop-punching is unsuitable. It has been noted that a vacancy flux from some prolific source would be necessary to avoid the generation of extremely large stresses. If it should happen that the total vacancy flux is insufficient, an interface perturbation having a small radius of curvature might be able to punch loops, relieve local stresses, and grow.

Finally, as an extreme case, if the vacancy flux were insufficient and loops were not generated, the stresses could well exceed the elastic limit and an incoherent -- even pseudo-liquid-boundary could develop. Such a layer would certainly allow extensive shuffling during rapid growth; such a layer has never been observed and would not likely be more than a few atom layers in thickness. In cases where the interface advances by the lateral motion of steps, such a layer is unlikely.

4.2 Vacancy Sources

Thermal Vacancies

It is well known that the fraction of lattice sites occupied by vacancies is of the form $\exp(S^f/k) \exp(-H^f/kT)$ in which S^f and H^f are

the entropy and enthalpy of vacancy formation. Upon quenching from T_1 to T in such a way that no vacancies are lost to sinks, the crystal contains $n(T_1)$ vacancies; but the equilibrium number is n(T). Choosing $\exp(S^f/k) = 10$, $H^f = 0.9$ eV/atom, $T_1 = 773^oK$, and $T = 573^oK$, it is found that the excess number of vacancies per lattice site is 1.72×10^{-5}.

The number of thermal vacancies per original lattice site required to completely relieve the volume strain $\Delta V/V$ is $\Omega\Delta V/\Omega_o V$ where Ω is the mean atomic volume and Ω_o is the vacancy volume taken as $\Omega/2$. Thus, for a volume strain of 0.026, the number of vacancies required would be 5.2×10^{-2} per site. Clearly, thermal vacancies are an inadequate source unless T_1 is considerably higher than the growth temperature T.

Thermal Contraction

In the case of a polycrystal, inhomogeneous thermal contraction could lead to the creation of very large numbers of vacancies at grain boundaries but these would likely react to form stable voids and would not be available for strain relaxation.

Climbing Dislocations

An edge dislocation $\frac{a}{2}[111]$ of length L in a b.c.c. lattice climbing through a distance h liberates $2hL/a^2\sqrt{6}$ vacancies. (4.18)

Typical dislocation densities in annealed and cold-worked metals are 10^6 and 10^8 cm/cm^3. Hence the numbers of vacancies liberated per original lattice site are $ah \times 10^6/\sqrt{6}$ or $ah \times 10^8/\sqrt{6}$. Taking the maximum climb distance as about one half the grain size -- say 0.01 cm -- and the lattice parameter as $3\mathring{A}$, the figures become 1.2×10^{-4} and 1.2×10^{-2}.

It appears that climbing dislocations could account for a sufficient number of vacancies to at least partially relieve a volume strain of 0.026. In fact, the dislocation density could be further increased by the action of loop mills such as Bardeen - Herring sources (59). However, it must be emphasized that only dislocations lying in the more intense regions of the stress field are motivated to climb and this fact severely restricts the effective density of climbing dislocations. Finally, the climb velocity being proportional to the climb force, decreases as volume relaxation proceeds so that climb cannot completely relieve the stresses.

Climbing interface dislocations can make an appreciable contribution to relaxation only when the extra half-planes lie in the growing phase and when mismatch is large. Moreover, they are restricted to climb at the same rate as the interface advances.

Surfaces

An internal surface such as a high angle grain boundary can act as a source of vacancies providing its area is reduced, since a simple translation does not liberate any vacancies. The importance of internal surfaces as sources is seen to decrease with increasing grain size.

On the other hand, an external surface has an infinite capacity and is apparently limited only by the large source-to-sink distances usually encountered. It may be that surface vacancies diffuse into the crystal as individuals (Herring-Nabarro creep) or as groups (prismatic dislocation glide) as shown in Figure 20. Indeed prismatic loop punching followed by glide to an external surface would appear to be the most

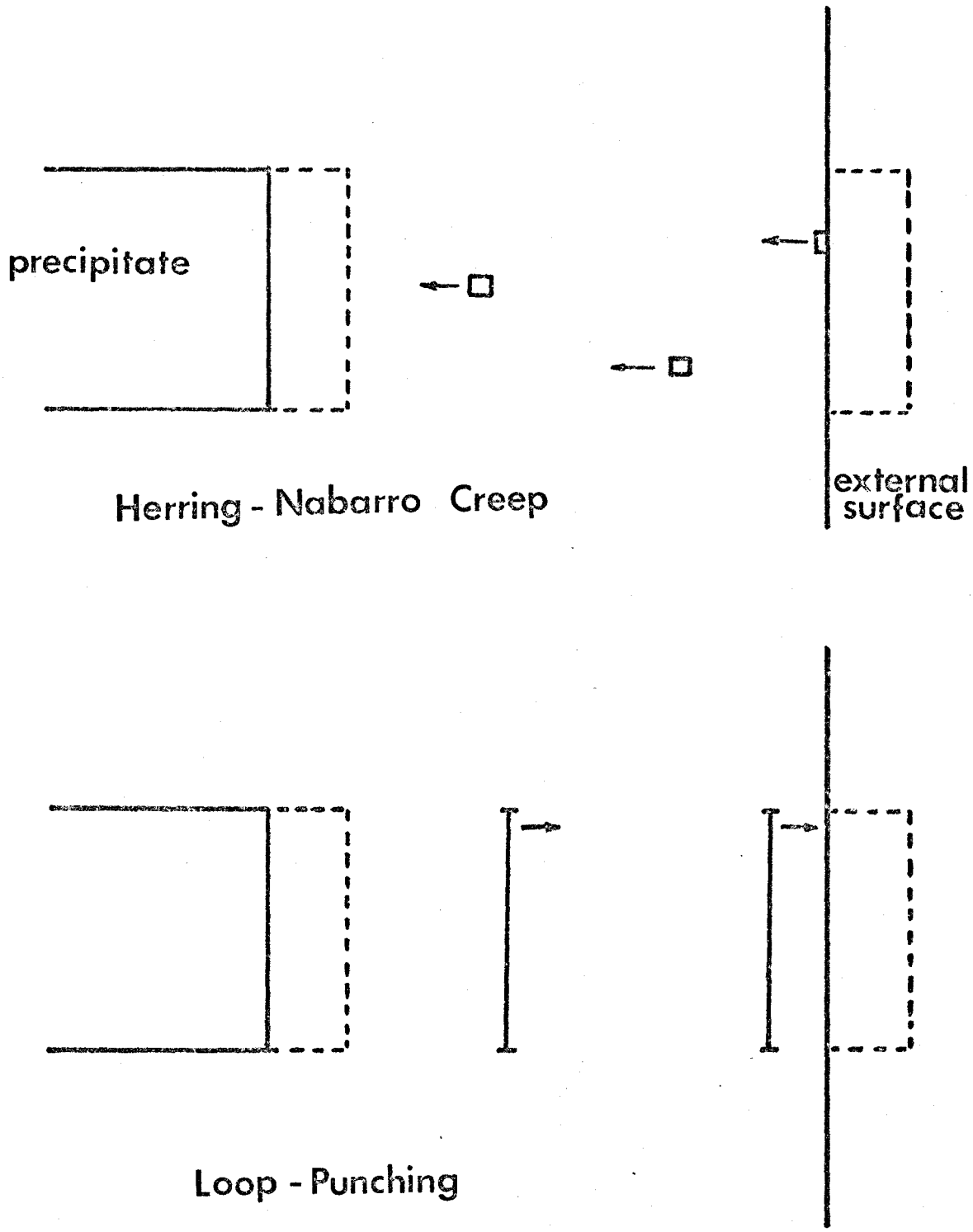

Figure 20. Relaxation Mechanisms

favourable mechanism for volume strain relaxation. Yet the presence of pinning bodies such as other precipitates, internal surfaces, and dislocation tangles would lead to entrapment of loops before they could reach the surface. In cases where loops are trapped in heavily defected crystals, the climb process is probably the major vacancy source.

4.3 The Role of Interface Dislocations in Precipitate Growth

Depending upon the sign of the misfit, theextra half plane of atoms can be either in the matrix or the precipitate. It is much easier for a dislocation to climb down rather than up since the former emits vacancies while the latter must absorb them and of necessity this requires an active source nearby. The question of sources has already been treated. One must conclude that in a real system, downclimb is far the more rapid process.

As observed by Aaronson (7) the motion of semicoherent interfaces is restricted by the condition that the interface dislocations must climb in unison at the interfacial rate of advance. The climb rate of a dislocation absorbing $\dot{n}$ vacancies per second at its core is $b^2\dot{n}$. The Kirkendall flux from equation (4.8) is $\nu(\frac{1}{\Omega''} - \frac{1}{\Omega'})$ normal to the interface. To calculate the number of vacancies entering the dislocation core, one must integrate J_0 over a "capture surface" defined as the surface bounding the region wherein the chemical potential μ_0 of a vacancy is altered by a term not less than the thermal energy kT (see Figure 21).

This requirement insures that when a vacancy drifts across the capture surface it will not be able to escape but will diffuse up the

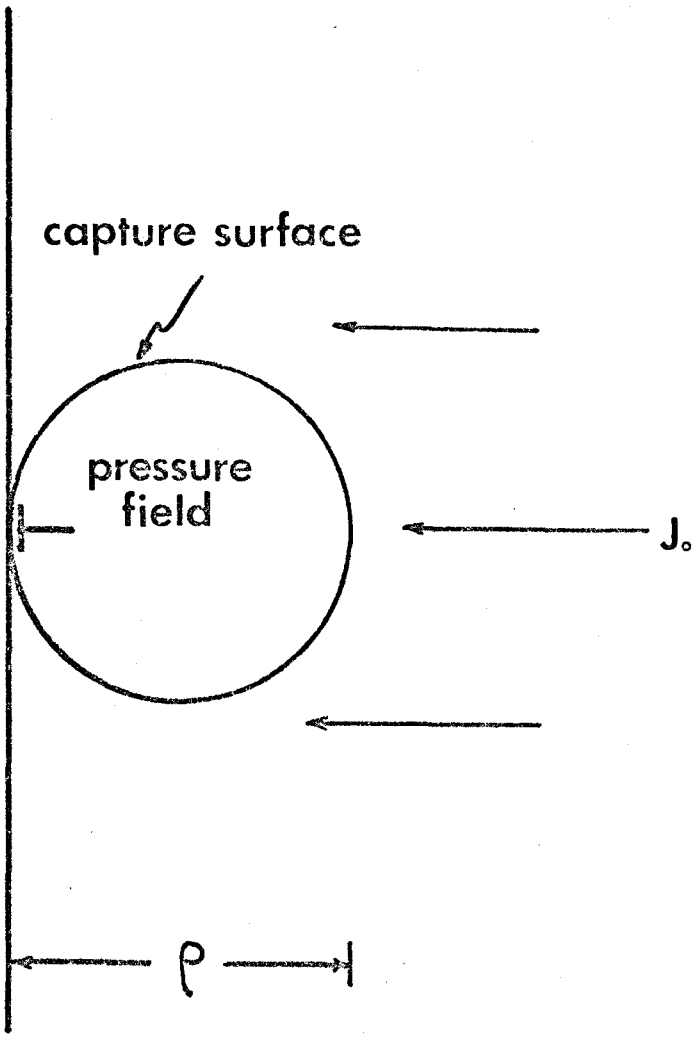

Figure 21. Climb Assisted by Kirkendall Flux

pressure gradient to the core. The pressure-volume term in vacancy chemical potential is $p\Omega_o = \Omega_o \frac{\mu b(1+\nu)}{3\pi(1-\nu)} \frac{\sin\phi}{r}$ (4.19)

When $r = \rho$ at $\phi = \frac{\pi}{2}$, set $p\Omega_o$ equal to kT and solve for ρ. The resulting capture radius is

$$\rho = \frac{\mu b(1+\nu)\Omega_o}{3\pi(1-\nu)kT} \tag{4.20}$$

The equation of the capture surface is $r = \rho \sin\phi$. Hence,

$$\dot{n}_o = 2\int_{\frac{\pi}{4}}^{\frac{\pi}{2}} J_o \rho \sin\phi \, d\phi$$

$$= \sqrt{2}\, J_o \rho$$

$$= \nu\left[\frac{\sqrt{2}\,(1+\nu)}{3\pi(1-\nu)} \frac{\mu b}{kT} \left(\frac{\Omega_o}{\Omega''} - \frac{\Omega_o}{\Omega'}\right)\right] \tag{4.21}$$

Finally, the dislocation climb rate is related to ν by

$$\nu_\perp = \nu\left[\frac{\sqrt{2}}{3\pi} \frac{(1+\nu)}{(1-\nu)} \frac{\mu b^3}{kT} \left(\frac{\Omega_o}{\Omega''} - \frac{\Omega_o}{\Omega'}\right)\right] \tag{4.22}$$

When $\nu_\perp < \nu$, the dislocations act as pinning points to retard growth. If a ledge containing a disordered segment is responsible for growth, then as Aaronson point out, the interface could advance fairly rapidly and remain macroscopically planar. In the absence of ledges, the build-up of pressure and volume free energy would lead to an enhancement of the vacancy flux.

However, it is possible that the interface might bulge outward between the pins. This would be equivalent to nucleating a perturbation of wavelength equal to the inter-dislocation spacing. The same conclusion

can be reached by replacing the constant surface free energy γ in the standard perturbation analysis with one having the periodicity of lattice misfit. The surface strain energy is indeed localized to the vicinity of dislocations. The result is analogous to that of Cahn (5): the perturbation reflects the interface symmetry. In some of Malcolm's photographs, dislocations are observed at troughs in γ precipitates and there may well be some connection as suggested above.

4.4 Discussion of Results

The Kossel photographs confirm that grain boundary γ actually grows into the β grain with which it is coherent. Apparently, the Smith hypothesis (13) was proposed somewhat hastily since there is now ample evidence that grain boundary precipitates can grow into the grain with which they are coherent, or the incoherent grain, or both.

Moreover, the observation of the breakdown of nearly coherent interfaces indicates that these must be much more mobile that was heretofore assumed. This, correlated with the fact that the maximum mobility accompanied the minimum mismatch and surface free energy suggests that, instead of classifying coherent interfaces as immobile, one should consider the amount of strain at the interface and the type of dislocations present there. Dislocations with some screw character -- like those observed by Nicholson and Weatherly (18) -- present the possibility that the ledge-motion growth process could be enhanced by the operation of growth spirals. Pure edge dislocations would require ample vacancy fluxes or the lateral motion of ledges (7) for interface advance; an interface containing edge dislocations should be much less mobile than

one containing screws for low supersaturations when lateral growth dominates. Even less mobile is an interface containing sessile partial dislocations which can neither climb nor glide.

Although not enough photographs are available for analysis, one qualitatively observes that the perturbation wavelength (typically 1 micron) decreases as the aging temperature decreases. So many quantities are temperature-dependent that any attempt to ascribe the increase in wavelength to any one of them is hazardous; but it is probable that the change is due to a larger gradient caused by increasing supersaturation and a rapidly decreasing diffusivity.

On specimen C annealed at 400^{o}C for microprobe work, very long, tenuous stringers of γ were observed -- usually starting from grain boundaries. It is believed that these represent precipitates formed on subgrain boundaries and having almost zero specific surface free energy. For such a low surface energy, the driving force for spheroidization is quite small and these stringers are thermally stable since they replace an incoherent subgrain boundary.

Concerning the flower morphology, it has already been suggested that the petals represent dendrites along <111> directions corresponding to the most favoured slip directions in bcc. Alternatively, one may compare Figures 10(d) and 11(d) in which pre-equilibrated dodecahedra bounded by {110} faces are breaking down at regions of high curvature (irrational planes). Unless one is prepared to assume that the flowers were nucleated in the equilibrium dodecahedral form it is not logical that Figures 10(d) and 11(d) portray the evolution of the dendrites forming petals. They do indicate that the dendrites are crystallographically

oriented as is obvious from many of the optical micrographs.

The sine-wave shape of interface perturbations seems to check with Sekerka's time-dependent theory (23) in which the form of the initial perturbation does not appreciably influence the final (sinusoidal) state. Furthermore, the value of γ obtained from analysis of the fastest-growing wavelength turns out to be the same order of magnitude as that estimated from dihedral angle measurement and that predicted from the dislocation model.

Finally, the mobility of these interfaces can be estimated by taking the velocity equal to peak height divided by aging time and, by fitting a parabola to Cox's (61) free energy-composition curves, the free energy change for transformation of supersaturated β to equilibrium $\beta + \gamma$ may be estimated. The results are: For a velocity of 6.7×10^{-7} cm/sec. under a driving force of about 3 cal/mole, the mobility is of order 5×10^{-15} mole. cm/erg.sec. This is within a factor of 5 of the mobilities reported by Shapiro (62) for incoherent grain growth in Cu-Zn and indicates that this semicoherent interface has mobility comparable to an incoherent one.

CHAPTER 5

SUGGESTIONS FOR FUTURE WORK AND CONCLUSIONS

Of primary importance is the need for some transmission electron microscopy to reveal the nature of interface dislocations in β/γ brass. Their Burgers vectors and spacings could be compared with those predicted by the model to deduce the amount of uncompensated elastic strain and the nature of their motion.

The action of a moving interface to sweep up defects in cold-worked material would be of interest to explain the apparently high perfection of the precipitate and the source of the interfacial dislocations

In a different line, measurements of the elastic constants of γ brass would lead to a more refined estimate of surface energy leading to a more accurate γ-plot.

Measurement of kinetic data would be useful to compare observed growth rates with those expected for volume-diffusion-controlled growth enabling one to estimate the effect of dislocation drag on growth kinetics. A study similar to that of Laird and Aaronson (17) would be an excellent complement to the work presented here.

Briefly stated, the present project has provided a dislocation model for semi-coherent interfaces in β/γ Cu-Zn-Sn which predicts reasonable values of interfacial free energy suggesting that the equilibrium form is a dodecahedron.

The numerical value of the surface energy, about 35 ergs/cm^2 is in good agreement with that deduced from dihedral angle measurements and from measurement of the (apparent) fastest-growing perturbation wavelength. This last observation lends support to the time dependent theory of Sekerka.

Quench - and -age heat treatments reveal extensive interface instability in Cu-Zn-Sn alloys. The maximum instability coincides with the minimum lattice mismatch indicating that fully coherent interfaces, in this case, have quite large mobilities contrary to Smith's popularly-held hypothesis that they should not. Further, it was shown that allotriomorphs grew into the grain with which they were coherent indicating that no sweeping statement can be made to predict into which grain an allotriomorph will grow.

It is hypothesized that the generation of volume strain on transformation favours the nucleation and growth of perturbations when the vacancy flux to the interface is insufficient. This is employed to rationalize the "flower" morphology observed in freshly-nucleated precipitates of this system.

Finally, one is forced to admit that much, much more work is needed before we begin to understand the complex nature of even a simple phase transformation.

APPENDIX I

LATTICE PARAMETERS FROM KOSSEL DIFFRACTION

The method involves measuring the half angle ε subtended on the film by a pair of intersecting conics. On Figure 22, CG is the lens length measured on the film, D is the specimen-to-film distance, O is the film centre, and α and β are the angles measured from the film normal.

Generally,

$$CG = D\,[(\sec\alpha + \sec\beta)^2 - 4\sec\alpha\sec\beta\cos^2\varepsilon]^{1/2} \qquad (I.1)$$

The cubic lattice parameter can be written

$$a = f\sec\varepsilon \qquad (I.2)$$

in which f is a function of wavelength, the indices of the planes forming the cones which define the lens, and the angles α and β. The problem becomes one of measuring ε accurately in an experiment where f is tractable. Three methods of doing this require either:

(a) $\alpha = \beta = \varepsilon$ (tangential case)

(b) $\alpha = \beta \neq \varepsilon$ (isosceles case) or

(c) $\beta = \alpha + 2\varepsilon$ (radial case)

All these methods require either extraordinary good fortune or a great deal of tilting and rotating plus a means of very accurately marking the film centre.

The method proposed by Hanneman et al. (48) is very attractive

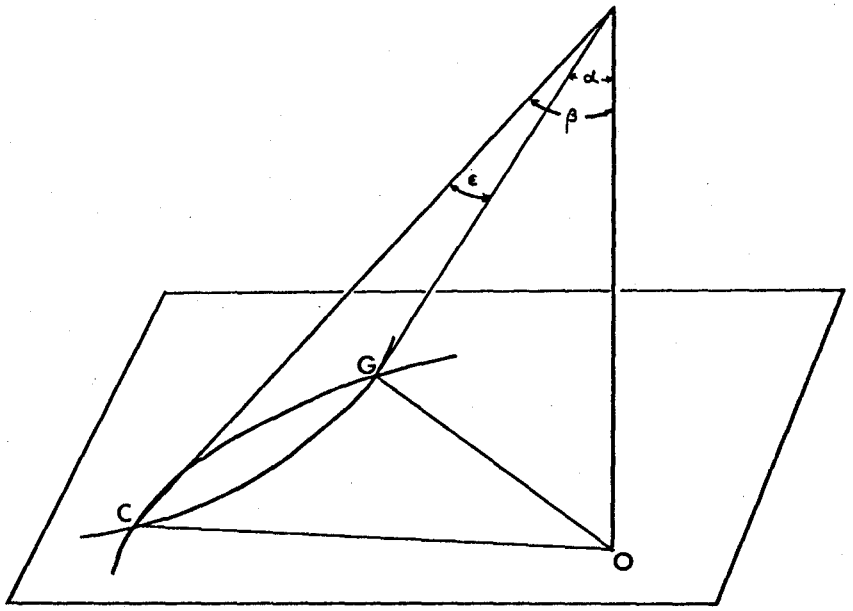

Figure 22. Kossel Geometry

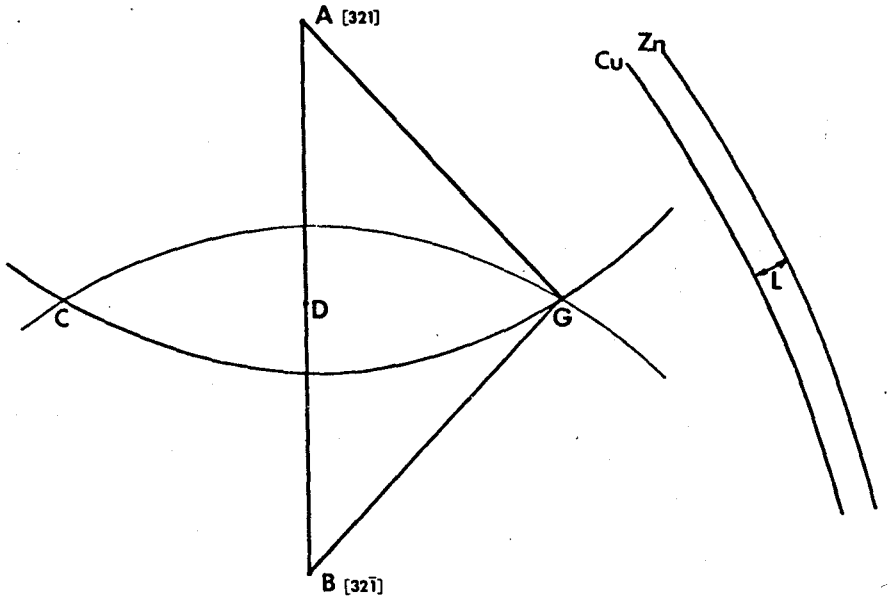

Figure 23. Lattice Parameters following Hanneman

since all of the above restrictions are relaxed. Furthermore, since it is an iterative method, quite high precisions -- the order of 10 ppm -- are attainble. When follows is a development of the equations used to determine the lattice parameter of brass using the intersection of two {321} cones. The proof closely follows reference (48). Consider Figure 23.

From Bragg's law

$$\cos AC = \sin\theta_{321} = \frac{\lambda\sqrt{14}}{2a} \tag{I.3}$$

and

$$\cos BC = \sin\theta_{32\bar{1}} = \frac{\lambda\sqrt{14}}{2a}$$

From geometry,

$$AB = \cos^{-1}\frac{6}{7} = \delta \tag{I.4}$$

From spherical trigonometry,

$$\cos AD \cos CD = \frac{\lambda\sqrt{14}}{2a} \tag{I.5}$$

and

$$\cos BD \cos CD = \frac{\lambda\sqrt{14}}{2a}$$

Also BD = AB - AD so that

$$\cos (AB-AD) = \cos AB \cos AD + \sin AB \sin AD$$

and AD = AB - BD so that (I.6)

$$\cos (AB-BD) = \cos AB \cos BD + \sin AB \sin BD$$

Add equations (5), let CD = ε, and substitute equations (6) to find

$$\cos \varepsilon \,[\cos \delta \,(\cos AD + \cos BD) + \sin \delta \,(\sin AD + \sin BD)] = \frac{\lambda\sqrt{14}}{a} \tag{I.7}$$

Recalling the formula for sum of sines and sum of cosines and noting that

$$AD + DB = \delta$$

and (I.8)

$$AD - DB = 0$$

equation (7) becomes,

$$\cos \varepsilon \left[\cos \delta \cos \frac{\delta}{2} + \sin \delta \sin \frac{\delta}{2}\right] = \frac{\lambda\sqrt{14}}{2a} \qquad (I.9)$$

Substituting for δ and λ of $CuK\alpha_1$ corrected for refraction (I.9) becomes

$$a = \frac{0.770263\ \sqrt{14}}{0.98199} \sec \varepsilon \qquad (I.10)$$

To determine ε, use is made of a natural standard: the separation of the $CuK\alpha_1$ and $ZnK\alpha_1$ cones of a given pole. Starting from an approximate a one can calculate the difference $\Delta\Theta$ in Bragg angles for the two wavelengths and compute a first ε using measured lengths:

$$\frac{CG}{L} = \frac{\sin \varepsilon}{\sin \frac{1}{2} \Delta\Theta} \qquad (I.11)$$

With the ε obtained here, one can recalculate a and repeat the procedure. Iteration is continued until the sequence converges.

In the experiment, the lines defining L were the $CuK\alpha_1$ and $ZnK\alpha_1$ conics of a 110 reflection passing through the middle of the lens. A binary Cu-Zn specimen annealed at 650°C for 24 hours was polished to a suitable thickness as described before and Kossel patterns from β were obtained and measured using a travelling microscope. The results appear in Table I-1.

TABLE I-1

KOSSEL MEASUREMENTS

CG (cm)	L (cm)	a_o (Å)
$2.8394_{\pm 5}$	$0.3276_{\pm 5}$	2.9552
2.8417	0.3272	2.9553
2.8422	0.3276	2.9555
2.8152	0.3224	2.9557
2.8126	0.3206	2.9540

Error Analysis

The relative error in a is

$$\frac{da}{a} = \frac{d\lambda}{\lambda} + \frac{\tan \varepsilon}{\cos \varepsilon} \, d\varepsilon \qquad (I.12)$$

From equation (11),

$$\frac{\cos \varepsilon \, d\varepsilon}{\sin \varepsilon} = \frac{dCG}{CG} + \frac{dL}{L} \qquad (I.13)$$

Combining (12) and (13) and letting $d\lambda$ approach zero, one obtains,

$$\frac{da}{a} \approx \frac{\tan^2 \varepsilon}{\cos \varepsilon} \left[\frac{dCG}{CG} + \frac{dL}{L} \right] \qquad (I.14)$$

Typically, ε is about 7^o, so for the data in Table I-1

$$\frac{da}{a} \approx 0.014 \left[\frac{5}{3} \times 10^{-5} + \frac{5}{3} \times 10^{-4}\right)$$

$$\approx \text{the order of a few ppm}$$

The factor $\frac{\tan^2 \varepsilon}{\cos \varepsilon}$ is what gives the Kossel method its great precision. The greatest error source is lens measurements. High-contrast lines of narrow width are required as well as a good travelling microscope unless enlarged prints can be made.

APPENDIX II

CORRECTION OF WAVELENGTHS

The wavelengths of $CuK\alpha_1$ and $ZnK\alpha_1$ in vacuo reported by Barrett and Massalski (49) are

$$\lambda_o = 1.540562_{\pm 5}\ \text{Å} \quad \text{and} \quad 1.435155_{\pm 5}\ \text{Å}$$

According to Wilson (60) the index of refraction except near absorption edges is

$$1 - \frac{\mathcal{A} e^2 \lambda^2 \rho}{2\pi m_o c^2} \frac{\Sigma A_i}{\Sigma M_i} \qquad \text{(II.1)}$$

in which $\mathcal{A}$ is Avogadro's number, e is the electronic charge, m_o is the electronic rest mass, c is the velocity of light, ρ is the density of the medium, and A_i and M_i are the atomic number and atomic weight of species i with sums covering one unit cell. This becomes

$$\delta = 2.71 \times 10^{-6}\ \rho\ \lambda_o^2 \frac{\Sigma A_i}{\Sigma M_i} \qquad \text{(II.2)}$$

for ρ in gm. cm^{-3} and λ in Å. The corrected wavelength is

$$\lambda = \lambda_o\ (1 - \delta) \qquad \text{(II.3)}$$

The results of correction appear in Table II.1

TABLE II-1

CORRECTED WAVELENGTHS

Alloy	ρ	$\Sigma A_i/\Sigma M_i$	$\delta \times 10^5$	Cu: λ (Å)	Zn: λ (Å)
β brass	8.03	0.458	2.36	$1.540526_{\pm 5}$	1.435136
γ brass	8.02	0.456	2.34	1.540526	
nickel	8.86	0.477	2.71	1.540520	
copper	8.85	0.457	2.59	1.540522	

REFERENCES

1. Cahn, J. W., Acta Met. 8, 554 (1960).
2. Mullins, W. W., in Metal Surfaces; A.S.M. (1963).
3. Johnson, A. J. C., Surface Science 3, 429 (1965).
4. Shewmon, P. G., T.A.I.M.E. 233, 736 (1965).
5. Cahn, J. W., Proc. Int. Conf. Crystal Growth 681 (1967).
6. Dubé, C. A., Aaronson, H. I. and Mehl, R. F. Rev. Mét. 55, 201 (1958).
7. Aaronson, H. I. in Decomposition of Austenite by Diffusional Processes; Interscience, N. Y. (1962).
8. Mehl, R. F., and Marzke, O. T., T.A.I.M.E. 93, 123 (1931).
9. Kelly, A., and Nicholson, R. B., Prog. Mat. Science 10, 151 (1963).
10. Massalski, T. B., Acta Met. 6, 243 (1955).
11. Kittl, J. E. and Massalski, T. B., Acta Met. 15, 161 (1967).
12. Malcolm, J. A. and Purdy, G. R., T.A.I.M.E. 239, 1391 (1967).
13. Smith, C. S., T.A.S.M. 45, 533 (1953).
14. Clark, J. B. in High Temperature, High-Resolution Metallography; Gordon and Breach, N. Y. (1967).
15. Hren, J. A. and Thomas, G., T.A.I.M.E. 227, 308 (1963).
16. Laird, C., and Aaronson, H. I., Acta Met. 15, 73 (1967).
17. Laird, C., and Aaronson, H. I., T.A.I.M.E. 242, 1393 (1968).
18. Nicholson, R. B. and Weatherly, G. C., Phil. Mag. 17, 801 (1968).
19. Mullins, W. W. and Sekerka, R. F., J. Appl. Phys. 34, 323 (1963).
20. Mullins, W. W., and Sekerka, R. F., J. Appl. Phys. 35, 444 (1964).
21. Coriell, S. R. and Parker, R. L., J. Appl. Phys. 37, 1548 (1966).

22. Coriell, S. R. and Parker, R. L., Proc. Int. Conf. Cryst. Growth, 703 (1967).

23. Sekerka, R. F., J. Phys. Chem. Solids 28, 983 (1967).

24. Delves, R. T., Phys. Stat. Solidi. 16, 621 (1966).

25. Hardy, S. C., and Coriell, S. R. Not yet published.

26. Morris, L. R. and Winegard, W. C., J. Cryst. Growth, 1, 245 (1968).

27. Woo Shueling, Barrett, C. S. and Mehl, R. F., A.I.M.E. Tech. Pub. 1694, 1 (1944).

28. Turnbull, D., in Impurities and Imperfections; A.S.M. (1955).

29. Head, A. K., Phys. Stat. Solidi 6, 461 (1964).

30. Weertman, J., and Weertman, J. R., in Elementary Dislocation Theory; Macmillan, N. Y. (1964).

31. Stroh, A. N., Phil. Mag. 3, 615 (1958).

32. Eshelby, J. D., Read, W. T. and Shockley, W., Acta Met. 1, 251 (1953).

33. McManus, G. M., Phys. Rev. 129, 2004 (1963).

34. Hansen, M., in Constitution of Binary Alloys; McGraw-Hill, N. Y. (1958).

35. Hirth, J. P. and Lothe, J., in Theory of Dislocations; McGraw-Hill, N. Y. (1968).

36. Foreman, A. J. E., Acta Met. 3, 322 (1955).

37. Shewmon, P. G. and Robertson, W. D., in Metal Surfaces; ASM (1963).

38. van der Merwe, J. H., J. Appl. Phys. 34, 117 (1963).

39. Herring, C. in The Physics of Powder Metallurgy; McGraw-Hill; N. Y.(1951).

40. Swalin, R. C. in Thermodynamics of Solids, Wiley, N. Y. (1962).

41. Stephens, D. E., private communication.

42. Landergren, U. S., Birchenall, C. E. and Mehl, R. F., J. Met. 8, 73 (1956).

43. Lonsdale, K., Phil. Trans. Roy. Soc. 240 219 (1947).

44. Bevis, M. and Swindells, N., Phys. Stat. Solidi 20, 197 (1967).

45. Morris, W. G., J. Appl. Phys. 39, 1813 (1968).

46. Peter, E. T. and Ogilvie, R. E., T.A.I.M.E. 233, 82 (1965).

47. Bevis, M., private communication.

48. Hanneman, R. E., Ogilvie, R. E. and Modrzejewski, A., J. Appl. Phys. 33, 1429 (1962).

49. Barrett, C. S. and Massalski, T. B., in Structure of Metals, Third Edition; McGraw-Hill, N. Y. (1966).

50. Pearson, W. B., in Handbook of Lattice Spacings and Structures of Metals, Vol. I; Pergamon Press, London (1958).

51. Darken, L. S. and Gurry, R. W., in Physical Chemistry of Metals; McGraw-Hill, N. Y. (1953).

52. Li Che-Yu, Blakely, J. M. and Feingold, A. H., Acta Met. 14, 1397 (1966).

53. Mott, N. F. and Nabarro, F. R. N., Proc. Phys. Soc. (London) 59, 86 (1940).

54. Nabarro, F. R. N., Proc. Phys. Soc. (London) 59, 90 (1940).

55. Weatherly, G. C., Phil. Mag. 17, 791 (1968).

56. Brown, L. M. and Woolhouse, G. R., Phil Mag. 17, 781 (1968).

57. Jones, D. A. and Mitchell, J. W., Phil. Mag. 3. 334 (1958).

58. Eikum, A. and Thomas, G., Acta Met. 12, 537 (1964).

59. Bardeen, J. and Herring, C, in Imperfections in Nearly Perfect Crystals; Wiley, N. Y. (1952).

60. Wilson, A. J. C., in The Mathematical Theory of X-ray Powder Diffractometry; Philips, Eindhoven (1959).

61. Cox, G. W., Ph.D. Thesis, University of New South Wales (1965).

62. Shapiro, J. M., Ph.D. Thesis, McMaster University (1966).